



# Static floor field construction and fine discrete cellular automaton model: Algorithms, simulations and insights



Rong Huang<sup>a</sup>, Xuan Zhao<sup>a,\*</sup>, Chenyu Zhou<sup>a,\*</sup>, Lingchen Kong<sup>a</sup>, Chengqing Liu<sup>b</sup>, Qiang Yu<sup>a</sup>

<sup>a</sup> School of Automobile, Chang'an University, Xi'an 710064, China

<sup>b</sup> CISDI Engineering Co., Ltd., CISDI Group Co., Ltd., Chongqing 401120, China

## ARTICLE INFO

### Article history:

Received 11 April 2022

Received in revised form 4 August 2022

Available online 5 September 2022

### Keywords:

Pedestrian simulation

Cellular automaton

Static floor field

Discretization effect

Desired direction

Navigation

## ABSTRACT

While cellular automaton (CA) models have a broad range of applications in the field of pedestrian dynamics, there are still three significant issues (the efficient and accurate construction of the static floor field (SFF), the insufficient simulation accuracy, and the discretization effect) that have not been resolved or fully clarified yet. This work aims to tackle these challenges. First, a novel approximate algorithm that resolves the dilemma between accuracy and efficiency is proposed to construct the SFF, based on which the static navigation field is created by the proposed method. Then, a novel fine discrete CA model based on the desired direction is developed to capture the locomotion movement behaviour. The novel SFF construction algorithm and locomotion movement model are (theoretically and/or numerically) validated and compared to the state-of-the-art approaches in manifold scenarios. Later on, systematic simulation analyses are conducted to investigate the discretization effect at the micro and macro levels. The assessment metrics show that the performance of the proposed algorithm and model is superior over that of the state-of-the-art approaches. The proposed model can resolve the well-known diagonal movement artefact in the existing CA models and reproduce crowd movement and self-organized lane formation observed empirically. It is found that the non-isotropic SFF results in significantly biased and unrealistic evacuation movement. Moreover, the discretization degree is found to significantly affect the individual and crowd movement simulation outcomes, and the magnitude and direction of its effect depend on the used model and the setup of the scenarios. The proposed algorithm and model are promising tools in pedestrian modelling and simulation. The findings provide fresh insights into the development and application of CA models.

© 2022 Elsevier B.V. All rights reserved.

## 1. Introduction

Crowd simulation models have significant applications in various aspects such as evacuation planning and optimization [1], risk assessment and management [2], and thus are receiving more attention in recent decades due to the increasingly frequent mass events as a result of the growing population density in urban cities [3,4]. So far, different types of microscopic evacuation models have been developed, including, force-based models [5], agent-based models [6],

\* Corresponding authors.

E-mail addresses: [zhaoxuan@chd.edu.cn](mailto:zhaoxuan@chd.edu.cn) (X. Zhao), [cy-zhou@chd.edu.cn](mailto:cy-zhou@chd.edu.cn) (C. Zhou).

and rule-based models [7–9]. Among these models, cellular automaton (CA) models, as an importation branch of rule-based models, are known for the merits of flexibility, extendibility and computation efficiency [7,8] and thus have been widely used to simulate the evacuation behaviour at the operational level (e.g., large-scale simulation and real-time prediction) [10,11]. Thus, this paper focuses on CA models.

Some well-known deficiencies (e.g., the unrealistically diagonal movement trajectory) are limiting the applicability of the floor field (FF) CA model and other CA models to sophisticated behaviour modelling and simulations [12,13]. The non-isotropic static floor field (SFF) is one of the significant sources of these problems [12], in which not all the (negative) gradient directions of the SFF values of the lattice sites point to the exits. The SFF construction algorithms include two categories, i.e., the approximate algorithm and the exact algorithm. Kirchner and Schadschneider [14] first proposed to respectively use the Manhattan distance and the Chebyshev distance to approximate the minimum Euclidian distance based on the flood fill algorithm [15] (a cell iteration algorithm with high computation efficiency) in the SFF construction. These two distance measures respectively correspond to the Neumann neighbourhood and Moore neighbourhood algorithms, which both generate the non-isotropic SFF. To improve the approximation accuracy, Varas, et al. [16] used a linear combination of the Manhattan distance and the Chebyshev distance to construct the SFF. However, their algorithm suffers from a high computation burden. To resolve it, Huang and Guo [17] refine the implementation procedures to propose an approximate algorithm that achieves a similar accuracy but with a significantly lower computation load. Nevertheless, both their algorithms produce a coarse approximation of the Euclidian distance and thus result in the non-isotropic SFF. In terms of the exact algorithm, Nishinari, et al. [13] proposed to use the Dijkstra algorithm (an exact shortest path algorithm [18]) to calculate the minimum Euclidian distance. Though this exact algorithm can construct an (approximate) isotropic SFF, it is particularly time-consuming due to the high computation complexity of the Dijkstra algorithm and thus cannot meet the demand of large-scale simulation, especially for real-time state estimation and prediction. Therefore, how to efficiently and accurately construct the SFF in CA models is of critical importance and unresolved yet (*question 1* – the efficient and accurate construction of the SFF).

Apart from the non-isotropic SFF, whether there is any hidden factor that also contributes to the deficiencies in the existing CA models deserves further investigation. In the past decades, while a rich body of CA variants with different behavioural rules has been developed, most of them keep the core idea of the original CA model [8], that is, the self-driven element (i.e., the desired direction) that mimics the internal motivations of pedestrians in continuous models (e.g., social force model [5]) is completely simplified and then the SFF is used to formulate pedestrian movement. Its original purpose is to reduce the computation burden, with the expense of overlooking the subjective motivations of individuals in locomotion decision-making. This simplification could also contribute to the aforementioned problems (e.g., the diagonal movement artefact, demonstrated by our results). Moreover, though the capability of the existing CA models to simulate the conscious locomotion movement has been validated in various cases, most of them are not quantitatively calibrated and/or validated in respect of lane formation, which is one of the significant self-organized collective phenomena observed empirically [19]. Recently, some studies have successfully exploited the advantageous elements of continuous models to improve the performance of CA models (e.g., the concept of force [20]). Thus, we raise a question as to how to incorporate the desired direction of pedestrians into CA models by a straightforward and efficient means and whether this will facilitate more accurate evacuation behaviour modelling (*question 2* – the insufficient simulation accuracy of the existing CA models).

In traditional CA models, a pedestrian is modelled as an agent that occupies one cell, the size of which corresponds to the typical area occupied by a pedestrian in real life (e.g., 0.4 m × 0.4 m [21]). While these models are capable of reproducing the empirical observations in various scenarios, they have long been criticized for the coarse discretization of space and time because such a simplified operation creates significant limitations including an unrealistic velocity distribution and an inaccurate representation of the geometrical structures. Kirchner, et al. [22] first realized this problem and pointed out the potential advantages of finer spatial discretization. Also, an improved FFCA model with a higher spatial resolution is proposed. Subsequently, inspired by their findings, a body of fine discrete models has been developed and used to study the evacuation from different scenarios (e.g., [7,9,20,23–25]). These studies demonstrate the benefits of finer discretization for more realistic evacuation behaviour modelling in CA models. To increase and assess the performance of crowd simulation models, it has been a growing consensus that they should be calibrated and validated by empirical data in multiple motion base cases before practical applications [26,27]. From this perspective, finer discretization significantly increases the computation time of simulations, which leads to a serious challenge for the calibration and validation procedures. A straightforward way to resolve it is to use a relatively coarse discretization in the calibration and validation. On the other hand, due to the difficulty of collecting the data-sets eligible for model calibration and validation in complex infrastructures, the models calibrated and validated by using the motion base cases are often directly applied to the simulations related to complex infrastructures in practice (e.g., [28,29]). To this end, the discretization degree of the models usually has to be adjusted to accurately represent the complex structures. A question related to these two aspects arises as to whether the simulation outcomes obtained with the specific degree of spatial discretization are transferable to the situations where different degrees of spatial discretization are used. Essentially, this question concerns whether or not spatial discretization will influence pedestrian dynamics in simulations (*question 3* – the discretization effect).

In contrast to the extensive applications of fine discrete models, only four studies have focused on this question (*question 3*) in literature (to the author's best knowledge). More importantly, these studies have not shown a complete consensus on the answer to this question yet. Kirchner, et al. [22] first recognized the discretization effect and investigated

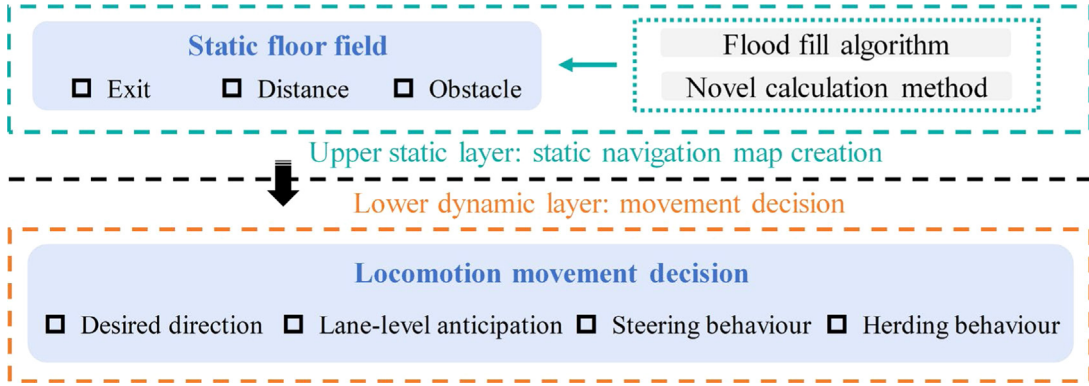


**Fig. 1.** Overview of the proposed algorithm and model. In each blue box, the sub-items are the main elements included. And, each grey box represents a component.

it in a large room with a narrow exit. They found that spatial discretization has a significant effect on the dynamical properties of the FFCA model. In a similar scenario, based on the proposed multi-grid model, Xu, et al. [30] observed that the evacuation time first increases with the discretization degree and then saturates, and that the discretization effect is closely related to the update rule. In a square room with an exit, Guo [31] found that the discretization degree not only has a non-monotonic effect on the average and total evacuation times, but also influences the crowd shape near the exit, by using the developed model. After summarizing the previous works, Fu, et al. [7] suggested that the behavioural rules deviated from the empirical observations would lead to biased simulation results. By using the proposed fine discrete FFCA model, they investigated the effect of spatial discretization on the evacuation from a room and found that the discretization degree has little effect on the total and average evacuation times. To sum up, in the existing four studies, the discretization effect has been only discussed in one type of evacuation scenario (i.e., a room with one exit). Due to largely inconsistent evidence as to the discretization effect, it is thus urgently necessary to systematically investigate it in more motion base cases (e.g., bidirectional flows) so as to thoroughly elucidate this question. On the other hand, the effect of spatial discretization on the individual movement simulation has been overlooked in literature, as opposed to the crowd movement simulation.

This paper aims to tackle these three issues. The main contributions are as follows: first, we put forward a novel approximate algorithm to efficiently and accurately construct the SFF. Second, a novel fine discrete CA model is developed, where the desired direction is introduced by a straightforward and efficient method based on the SFF to formulate pedestrian locomotion movement. Third, this paper for the first time systematically reveals the discretization effect at the microscopic and macroscopic levels by comparative simulation analyses using the proposed model and the state-of-the-art fine discrete CA model (i.e., [7]). The SFF approximate construction algorithm is theoretically and numerically validated by comparison with the exact algorithm (i.e., [13]) and the state-of-the-art approximate algorithms (i.e., [14–17]), and the locomotion movement model is validated by empirical data in various scenarios and compared to the state-of-the-art fine discrete CA model (i.e., [7]).

The structure of this paper is as follows: Section 2 proposes the SFF algorithm and the fine discrete CA model. Section 3 presents the setups of the simulations used to calibrate and validate the proposed algorithm and model, followed by the detailed results in Section 4. The key findings of this paper and recommendations for future research are concluded in Section 5.

## 2. Algorithm and model development

Fig. 1 gives an overview of the proposed algorithm and model. The upper layer corresponds to the SFF approximate construction algorithm, and the upper and lower two layers compose the fine discrete CA model. In the upper static layer, by integrating a novel calculation method and the flood fill algorithm [15], a new SFF approximate construction algorithm is proposed. In the lower layer, the static navigation field is first created by the proposed method to provide navigation directions for the locomotion movement decision of pedestrians. Then, with consideration of the steering behaviour, the desired direction of each pedestrian is determined. And, the velocity updating mechanism is introduced to reflect the acceleration and deceleration behaviour. Finally, pedestrians make a decision to determine the target movement direction by comprehensively considering the desired direction, the lane-level anticipation field and the dynamic floor field (herding behaviour). In the ensuing sections, these procedures will be illustrated in detail. The key notation is presented in Appendix A.

## 2.1. SFF construction algorithm

The proposed SFF approximate construction algorithm is denoted by **SFF-Construction**( $\alpha_{SF}$ ,  $\mathbb{C}$ ,  $ST^e$ ), shown in Algorithm 1. In lines 1–8,  $SD^{e,(i,j)}$  is calculated for all the cells in  $ST^e$ , the accuracy of which is controlled by parameter  $\alpha_{SF}$  ( $0 \leq \alpha_{SF} < +\infty$ ). And, the SFF value ( $SF^{e,(i,j)}$ ) of each cell is determined in line 9.

**SFF-Construction** ( $\alpha_{SF}$ ,  $\mathbb{C}$ ,  $ST^e$ ) uses a nonlinear combination of the Manhattan distance ( $NF^{e,(i,j)}$ ) and the Chebyshev distance ( $MF^{e,(i,j)}$ ) to approximate the minimum Euclidian distance, which is essentially different from the state-of-the-art approximate algorithms (i.e., [14,17]) where the Manhattan distance, the Chebyshev distance or a linear combination of them are used. Ascribed to this novel calculation method, when compared with the exact algorithm (i.e., [13]), the computation accuracy of the proposed algorithm with a proper value of  $\alpha_{SF}$  significantly outperforms the state-of-the-art approximate algorithms [14,17], as demonstrated in the theoretical proof (Appendix B) and numerical validation (Section 4.1). Nevertheless, as the flood fill algorithm is used [15], the proposed algorithm has the same computation complexity as the state-of-the-art approximate algorithms [14,17], i.e.,  $\mathcal{O}(N(ST^e))$  ( $N(ST^e)$  is the number of cells in  $ST^e$ ), whereas that of the exact algorithm [13] is  $\mathcal{O}(N(ST^e)^2)$ .

---

### Algorithm 1. SFF-Construction ( $\alpha_{SF}$ , $\mathbb{C}$ , $ST^e$ )

---

- 1: **For all** cells  $(i, j) \in ST^e$  **do**
  - 2:   Calculate  $NF^{e,(i,j)}$  and  $MF^{e,(i,j)}$  using the flood fill algorithm.
  - 3:    $QF^{e,(i,j)} \leftarrow (NF^{e,(i,j)} + MF^{e,(i,j)})/2$ .
  - 4:    $GF^{e,(i,j)} \leftarrow \sqrt{((MF^{e,(i,j)} + QF^{e,(i,j)})^2 + (NF^{e,(i,j)} + QF^{e,(i,j)})^2)/2}$ .
  - 5:    $RF^{e,(i,j)} \leftarrow 1/MF^{e,(i,j)}$ .
  - 6:    $CF^{e,(i,j)} \leftarrow 1 - \exp(-RF^{e,(i,j)} \cdot \alpha_{SF} \cdot GF^{e,(i,j)})$ .
  - 7:    $SD^{e,(i,j)} \leftarrow (1 - CF^{e,(i,j)}) \cdot MF^{e,(i,j)} + CF^{e,(i,j)} \cdot NF^{e,(i,j)}$ .
  - 8: **End for**
  - 9:  $SF^{e,(i,j)} \leftarrow \max_{(i,j) \in ST^e} \{SD^{e,(i,j)}\} - SD^{e,(i,j)}$ .
- 

## 2.2. Locomotion movement model

The proposed fine discrete CA model is dedicated to capturing locomotion movement behaviour and is based on three basic assumptions. First, a pedestrian is assumed to occupy a square area of  $R$  m  $\times$   $R$  m ( $R$  is set as 0.4) [21], which corresponds to  $n \times n$  cells. Second, each cell can be occupied by one pedestrian or obstacle at most (i.e., the exclusion-volume effect) [32]. Third, the free velocities of pedestrians follow Gaussian distribution, i.e.,  $N \sim (1.34, 0.34^2)$  [33].

Moreover, three commonly used basic rules in CA models are followed. Specifically, at each time step, pedestrians can stay still or move one cell towards one of the eight candidate directions, i.e., the Moore neighbourhood [8] is used. To reflect the conflict situations in real life, the movement of pedestrians is updated parallelly [34]. And, back steps are unallowable (i.e., the no-back-step rule) [34].

The proposed fine discrete CA model is depicted in Algorithm 2, denoted by **LM-Determination**( $ST^e$ ,  $SF^e$ ,  $F_{SN}$ ,  $F_{AF}$ ,  $F_{DF}$ ,  $t$ ). Compared with the existing CA models, the novelty of the proposed model mainly lies in the introduction of the desired direction in the movement decision through a straightforward and efficient method, which facilitates more realistic evacuation behaviour modelling, demonstrated in Section 4.2. To do this, the behavioural rules (e.g., the steering behaviour and the lane-level anticipation) are formulated by considering the desired direction. This to a large extent relies on the proposed SFF and navigation field construction methods.

In line 1, based on the SFF, the navigation direction ( $\vec{D}_A^{(i,j)}$ ) of each cell  $(i, j)$  is calculated by using the proposed method to construct the static navigation field. Line 2 initializes the desired direction of pedestrian  $q$ . At each time step  $t$ , pedestrian  $q$  has a probability  $P_S^q$  to steer to the (average) navigation direction of the occupied cell(s) (lines 4–6). In line 7, pedestrian  $q$  updates his/her velocity according to the surrounding environment. For each pedestrian  $q$  who is given the opportunity to update the position (line 8) [35], the lane-level anticipation field and the dynamic floor field values of all candidate direction  $\vec{D}^k$  that is reachable (i.e., the cell(s) in direction  $\vec{D}^k$  are not occupied by obstacles) are calculated in lines 10–11. With consideration of the desired direction, the lane-level anticipation field and the dynamic floor field, pedestrian  $q$  randomly chooses the target movement direction according to the transfer probability of each direction (lines 12–13). Lines 14–20 check the choice of each pedestrian and solve the conflicts so that only the eligible movement is implemented. Then, the dynamic floor field is updated according to the new position of pedestrians and the diffusion and decay rules [8] in line 22. Thereafter, the procedures in lines 3–23 are repeated until all pedestrians complete the evacuation. More details are described in the ensuing sections.

**Algorithm 2. LM-Determination( $ST^e$ ,  $SF^e$ ,  $F_{SN}$ ,  $F_{AF}$ ,  $F_{DF}$ ,  $t$ )**


---

1: Determine the navigation direction ( $\vec{D}_A^{(i,j)}$ ) of each cell  $(i,j)$  to construct the static navigation field according to the SFF.

2: Determine the desired direction ( $\vec{D}_P^q$ ) of pedestrian  $q$  according to his/her initial position  $(i_0, j_0)$ .

3: **For all** pedestrians  $q$  located in cell  $(i,j)$  at time step  $t$  **do**

4:   **If**  $rand() < P_S^q$  **then**

5:      $\vec{D}_P^q \leftarrow \frac{\sum_{i=1}^n \sum_{j=1}^n \vec{D}_A^{(i,j)}}{n^2}$ .

6:   **End if**

7:   Update  $v^{q,t}$ .

8:   **If**  $rand() < v^{q,t}/v_{\max}$  **then**

9:     **For all** directions  $\vec{D}^k$  reachable by pedestrian  $q$  **do**

10:       Calculate  $AF^{\vec{D}^k}$ .

11:       Calculate  $DF^{\vec{D}^k}$ .

12:       Calculate the transfer probability of moving towards  $\vec{D}^k$ .

13:       Randomly select a target movement direction  $\vec{D}^k$  for pedestrian  $q$  according to the transfer probability.

14:       **If** the target new position  $(i_N^k, j_N^k)$  is occupied by other pedestrians or  $\vec{D}_P^q \cdot \vec{D}^k < 0$  **then**

15:         Pedestrian  $q$  stays still.

16:       **End if**

17:     **End for**

18:   **End if**

19:   **For all** situations in which two or more pedestrians attempt to move into the same cell(s) **do**

20:     Randomly select one pedestrian to execute the movement.

21:   **End for**

22:   Update the dynamic floor field for all cells, which also diffuses with probability  $\alpha_{DF}$  (set as 0.1) and decays with probability  $\delta_{DF}$  (set as 0.05) [8].

23: **End for**

---

### 2.2.1. Constructing the static navigation field

Based on the SFF, the static navigation field is constructed by the following two steps.

**Step 1.** For all lattice sites  $(i,j) \in S_P$ ,  $\vec{D}_C^{(i,j)} \leftarrow \begin{cases} \left( SF^{(i+1,j)} - SF^{(i-1,j)}, SF^{(i,j+1)} - SF^{(i,j-1)} \right) & \#if N(\Omega_{NC}) = 8 \\ \frac{(x_{\min} - i, y_{\min} - j)}{\|x_{\min} - i, y_{\min} - j\|_2} & \#otherwise \end{cases}$ . Where  $(x_{\min}, y_{\min}) = \arg \min_{(x^l, y^l) \in S_P} \left\{ \sqrt{(x^l - i)^2 + (y^l - j)^2} \mid (x^l, y^l) = \arg \min_{(x^k, y^k) \in S_P} \left\{ SF^{(x^k, y^k)} \mid (x^k, y^k \in \Omega_{NC}) \right\} \right\}$ ;  $\Omega_{NC}$  is the set of cell  $(i,j)$ 's available neighbouring cells.

**Step 2.** For all lattice sites  $(i,j) \in S_P$ ,  $\vec{D}_A^{(i,j)} \leftarrow \arg \min_k \left\{ \vec{D}_C^{(i,j)} \cdot \vec{D}^k \mid k = 1, 2, \dots, 8 \right\}$ .

Through the above steps, the navigation direction ( $\vec{D}_A^{(i,j)}$ ) of each cell is calculated, which composes the static navigation field of the whole geometry structure. It should be noted that the accurate construction of the SFF is the basis of these procedures.

### 2.2.2. Determining the desired direction

At the beginning of the evacuation, the desired direction of pedestrian  $q$  depends on its initial position, calculated by Eq. (1).

$$\vec{D}_P^q = \frac{\sum_{i_0=1}^n \sum_{j_0=1}^n \vec{D}_A^{(i_0, j_0)}}{n^2} \quad (1)$$

Where  $(i_0, j_0)$  represents the cell(s) occupied by pedestrian  $q$  initially.

After moving to the new position, the desired direction of pedestrian  $q$  could deviate from the navigation direction of the occupied cells. And thus, at each time step, pedestrian  $q$  steers to the navigation direction with probability  $P_S^q$  as a

result of the inertia effect, given by Eq. (2).

$$P_S^q = \frac{\omega^q \cdot R}{n \cdot v_{\max} \cdot \theta_A} \quad (2)$$

With

$$\theta_A = \arccos \left( \frac{\vec{D}_P^q \cdot \vec{D}_C^q}{\|\vec{D}_P^q \cdot \vec{D}_C^q\|_2} \right) \quad (3)$$

Where  $\theta_A$  is the steering angle;  $\vec{D}_C^q = \frac{\sum_{i=1}^n \sum_{j=1}^n \vec{D}_A^{(i,j)}}{n^2}$ , where  $(i, j)$  is the current position of pedestrian  $q$ .

Eqs. (2) and (3) mean that the steering probability is positively and negatively correlated with the pedestrian angular speed and the steering angle respectively, which is logically understandable and complies with the previous works (e.g., [7,36]).

### 2.2.3. Updating the movement velocity

Empirical observations indicate that pedestrian movement velocity is influenced by the surrounding density [33,37–39]. One of the efficient ways to describe this characteristic is to incorporate the empirical velocity–density relationship into the pedestrian movement models so as to directly adjust the movement velocity (e.g., Liu, et al. [40]). The empirical formula from Weidmann [21] that is commonly used in literature is adopted here, shown in Eq. (4).

$$v^{q,t} = v_F^q \cdot \left( 1 - \exp \left( -\zeta \cdot \left( \frac{1}{\rho^{q,t}} - \frac{1}{\rho_{\max}} \right) \right) \right) \quad (4)$$

Where  $v_F^q$  is the free velocity of pedestrian  $q$ ;  $\zeta$  is a factor, equal to 1.913;  $\rho^{q,t}$  is the density within pedestrian  $q$ 's visual range (set as 2 m [41]) at time step  $t$ , and  $\rho_{\max} = 6.25$  persons/m<sup>2</sup> is the maximum density.

### 2.2.4. Computing the lane-level anticipation field

There is a common behaviour that pedestrians estimate the potential movement lane of others in front of them to avoid the potential collision in advance [42]. Thereby, the lane-level anticipation field is introduced to capture this behaviour. For a pedestrian  $q$ , there are three candidate movement lanes that can be chosen, i.e., the left lane ( $L_L$ ), the middle lane ( $L_M$ ) and the right lane ( $L_R$ ), shown in Fig. 2. The calculation of the lane-level anticipation field value is based on the movement lane of pedestrians. For each candidate movement direction, the corresponding target lane has to be first determined by Eq. (5).

$$\begin{cases} \text{sign}(\vec{D}_P^q \times \vec{D}^k) > 0 \# \text{The target lane is } L_L \\ \text{sign}(\vec{D}_P^q \times \vec{D}^k) = 0 \# \text{The target lane is } L_M \\ \text{sign}(\vec{D}_P^q \times \vec{D}^k) < 0 \# \text{The target lane is } L_R \end{cases} \quad (5)$$

Using candidate movement direction  $\vec{D}^1$  as an illustrative example, its lane-level anticipation field value is given by Eq. (6).

$$AF^{\vec{D}^1} = \frac{1}{N(\Omega_{L_M})} \sum_{(x_{L_M}, y_{L_M}) \in \Omega_{L_M}} \frac{\sum_{k=1}^{L_D} \lambda^{(k, \frac{R}{n})} \cdot \varepsilon \cdot f \left( \arccos \left( \frac{\vec{D}_P^q \cdot \vec{D}_P^{q'}}{\|\vec{D}_P^q \cdot \vec{D}_P^{q'}\|_2} \right) / \pi \right)}{\sum_{k=1}^{L_D} \lambda^{(k, \frac{R}{n})}} \quad (6)$$

Where  $\Omega_{L_M}$  is the set of the initial cells  $(x_{L_M}, y_{L_M})$  used to calculate the anticipation field value of lane  $L_M$ , shown in Fig. 2;  $L_D$  is the range of the lane-level anticipation field, set as  $\frac{8}{R} \cdot n$ ;  $\varepsilon$  is a binary variable (1, if  $(x_{L_M} + k \cdot x_{\vec{D}_P^q}, y_{L_M} + k \cdot y_{\vec{D}_P^q})$  is occupied by pedestrian  $q'$ ; 0, otherwise).  $x_{\vec{D}_P^q}$  and  $y_{\vec{D}_P^q}$  are respectively the horizontal and vertical coordinates of direction vector  $\vec{D}_P^q$ ;  $f \left( \arccos \left( \frac{\vec{D}_P^q \cdot \vec{D}_P^{q'}}{\|\vec{D}_P^q \cdot \vec{D}_P^{q'}\|_2} \right) / \pi \right)$  is a function, the value of which is equal to  $\arccos \left( \frac{\vec{D}_P^q \cdot \vec{D}_P^{q'}}{\|\vec{D}_P^q \cdot \vec{D}_P^{q'}\|_2} \right) / \pi$  when  $\frac{\pi}{2} \leq \arccos \left( \frac{\vec{D}_P^q \cdot \vec{D}_P^{q'}}{\|\vec{D}_P^q \cdot \vec{D}_P^{q'}\|_2} \right) / \pi$  and 0 otherwise;  $\lambda$  indicates the strength of the lane-level anticipation field, set as 0.8 [42].

### 2.2.5. Determining the movement direction

Real-life observations suggest that pedestrians usually choose the shortest route to evacuate, and tend to avoid the congested movement lane in advance, and follow the steps of the persons in front of them [43–45]. Thus, at each time step, pedestrian  $q$  makes the movement direction decision according to Eqs. (7)–(8).

$$P^{q,k} = \frac{M^{q,k}}{\sum_k M^{q,k}} \quad (7)$$

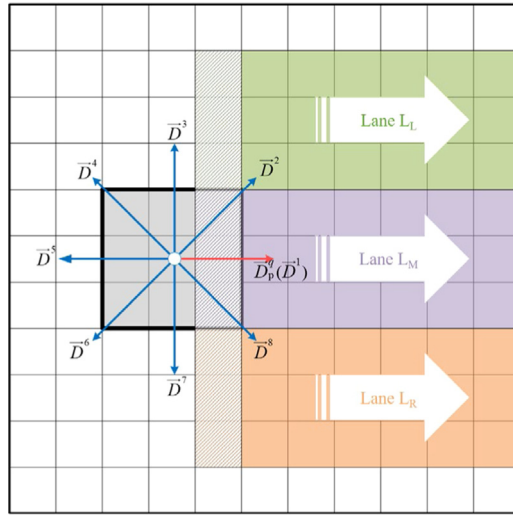


**Fig. 2.** Schematic diagram of the candidate movement lanes and directions (with the discretization degree  $n = 3$ ). For each lane, the hatched lines with the corresponding colour are superposed onto the initial cells used to calculate the lane-level anticipation field value.

$$M^{q,k} = \exp \left( F_{SN} \cdot \left( \frac{\vec{D}_P^q \cdot \vec{D}^k}{\|\vec{D}_P^q \cdot \vec{D}^k\|_2} + 1 \right) - F_{AF} \cdot AF^{\vec{D}^k} + F_{DF} \cdot \frac{\sum_{i^k=1}^n \sum_{j^k=1}^n B_{DF}^{(i^k, j^k)}}{n^2} \right) \quad (8)$$

Where  $P^{q,k}$  is the probability to move towards direction  $\vec{D}^k$  for pedestrian  $q$ ;  $(i^k, j^k)$  is the new position of pedestrian  $q$  if he/she moves towards  $\vec{D}^k$ .  $B_{DF}^{(i^k, j^k)}$  is the number of bosons in cell  $(i^k, j^k)$ .

$F_{SN}$ ,  $F_{AF}$  and  $F_{DF}$  are the three key parameters of the model, which will be calibrated by empirical data in Section 3.2.

### 3. Simulation setups

The simulation analyses include three parts

Part 1: (*question 1*): the parameter ( $\alpha_{SF}$ ) of the proposed SFF approximate construction algorithm is first calibrated by minimizing the errors deviating from the results of the exact algorithm (i.e., [13]). Then, as a complement to the theoretical proof of the computation accuracy in the geometry without obstacles (in Appendix B), numerical simulations are conducted in both geometries with and with obstacles to further demonstrate its computation and simulation accuracy advantage over the state-of-the-art approximate algorithms (i.e., [14–17]).

Part 2: (*question 2*): With the discretization degree  $n = 1$ , the proposed locomotion movement model is first calibrated and validated by using empirical data from various motion base cases, and then comparisons are conducted to demonstrate its performance advantage over the state-of-the-art fine discrete CA model (i.e., Fu et al.'s model [7]) in respect of simulating individual and crowd movement.

Part 3: (*question 3*): After model calibration and validation, comparative simulation analyses are conducted to investigate the effect of spatial discretization on the individual and crowd movement simulation outcomes by using our and Fu et al.'s models, so as to shed new light on the common characteristics and the underlying reasons of the discretization effect in CA models.

To avoid the influence of behavioural uncertainty [46], 500 and 30 runs are respectively repeated for each simulation in the first and the latter two simulation parts. Before simulation analyses, four parameters (see Table 1) of the algorithm and model are first calibrated by using the genetic algorithm (GA) [47] to search the parameter values that minimize the predefined error. In the process of calibration, the GA is designed to terminate when little reduction (<0.001) of the error has been detected for consecutive 10 rounds. This procedure is set to repeat 10 times, and the set of parameter values with the best fitness is eventually selected.

In the ensuing sections, the assessment metrics and the scenarios used for calibration, validation and simulation analyses are determined based on the well-established principles in [47–49].

#### 3.1. Part 1: SFF construction algorithm

Because pedestrian movement is almost deterministic in multi-obstacle spaces (e.g., theatres), the accuracy advantage of the SFF mainly reflects in simulating the evacuation in areas with sparse obstacles (e.g., shopping malls). Thus, two

**Table 1**  
Overview of the key parameters to be calibrated.

	Symbol	Meaning
SFF construction algorithm	$\alpha_{SF}$	SFF computation accuracy parameter
Locomotion movement model	$F_{SN}$ $F_{AF}$ $F_{DF}$	Sensitivity to the static navigation field Sensitivity to the lane-level anticipation field Sensitivity to the dynamic floor field

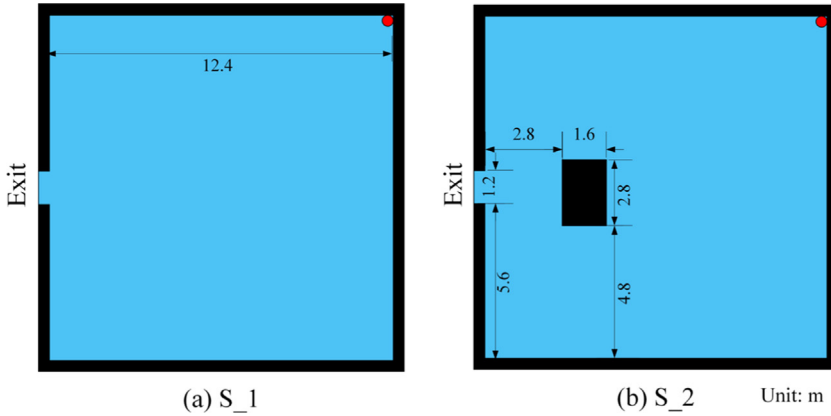


**Fig. 3.** Physical setups used for the calibration and validation of the proposed SFF construction algorithm.

types of scenes, i.e., a square room with (i.e., setup S\_1) or without (i.e., setup S\_2) an internal obstacle, are used as the illustrative examples, shown in Fig. 3.

First, GA is used to calibrate the value of  $\alpha_{SF}$  so as to minimize the average absolute error between the static floor fields constructed using our approximate algorithm and the exact algorithm [13] in setups S\_1 and S\_2, defined in Eq. (9):

$$\text{dist}_{SF} = \frac{1}{N_{SF}^1 N_{SF}^2 N_{SF}^3} \sum_{k=1}^{N_{SF}^1} \sum_{i=1}^{N_{SF}^2} \sum_{j=1}^{N_{SF}^3} |S_O^{k,i,j} - S_D^{k,i,j}| \quad (9)$$

Where  $S_O^{k,i,j}$  and  $S_D^{k,i,j}$  are respectively the SFF values of cell  $(i, j)$  in setup  $k$ , obtained by using our approximate algorithm and the exact algorithm [13].

Then, the main objective of the case studies is to show that when compared with the exact algorithm (i.e., [13]), **SFF-Construction** performs significantly better than the existing approximate algorithms (i.e., [14,17]) in terms of the SFF computation accuracy, and the microscopic (individual) and macroscopic (crowd) evacuation movement simulation accuracy, in both scenarios with and without obstacles.

Accordingly, three comparisons are conducted, shown as follows.

(1) SFF computation accuracy comparison. For each lattice site, the **absolute error (AE)** between the SFF values calculated using the approximate algorithm and the exact algorithm is computed, and the AE of the proposed algorithm is compared with those of the state-of-the-art approximate algorithms.

(2) Individual movement simulation accuracy comparison. The movement of a pedestrian located in the top-right corner of the room (the red circle in Fig. 3) to the exit is simulated. The **movement trajectories** and the **total movement times (TMT)** averaged over 500 runs are compared.

(3) Crowd simulation evacuation accuracy comparison. The crowd evacuation from the room filled up with pedestrians is simulated. The **total evacuation times (TET)** and the **mean of the individual evacuation times (MIET)** averaged over 500 runs are compared.

To ensure a fair comparison, the simulations of comparisons (2) and (3) are implemented using the original CA model developed by Kirchner and Schadschneider [14], with the SFF constructed by different algorithms. The used model parameter settings are shown in Table C.1 (Appendix C).

### 3.2. Part 2: Locomotion movement model

In the simulations of this part, the discretization degree  $n$  is set as 1. First, the model will be calibrated by using empirical data from several crowd movement experiments. Then, the capability of our model to resolve the diagonal movement artefact and reproduce the crowd movement behaviour observed empirically will be validated. Meanwhile, comparisons will be conducted to show its performance advantage over the model of Fu et al. in terms of the individual and crowd movement simulation.

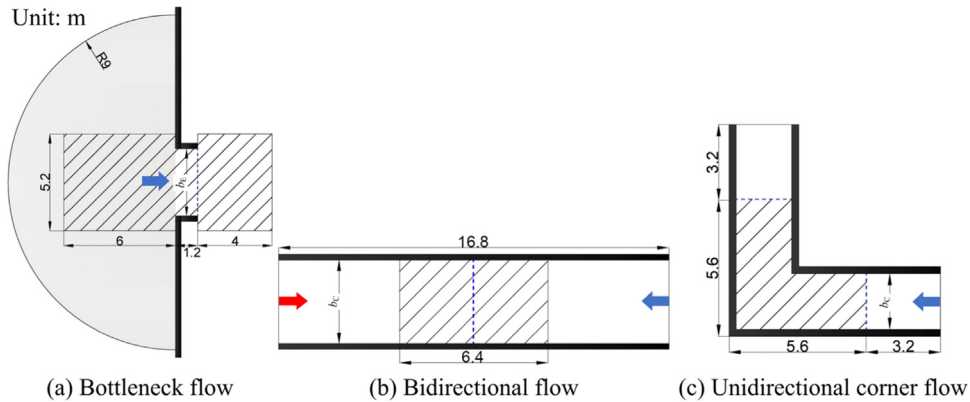


**Fig. 4.** Layout of the used three motion base scenarios. The hatched areas represent the measurement areas in experiments and simulations; the dashed blue lines indicate the location where the FR is measured and the grey area in (a) indicates the waiting area of pedestrians; the red and blue arrows indicate the flow directions.

**Table 2**

The experiments used for simulation analyses related to crowd movement [50], where the acronyms identify the purposes (i.e., VC = validation and comparison, Cal = calibration, SD = analyses related to the discretization effect) and the scenarios (i.e., Bi = bidirectional, Bo = Bottleneck, and Co = Corner).

Setups	Purposes	Original name in [50]	Scenarios	Density variants	$b_C$ (m)	$b_E$ (m)	$N$ ( $N_L/N_R$ )
M_1	Cal	AO-360-400	Bo	High	–	3.6	400
M_2	Cal	BO-360-160-160	Bi	High	3.6	–	300 (150/150)
M_3	Cal	EO-240-150-240	Co	High	2.4	–	100
M_4	VC and SD	AO-440-400	Bo	High	–	4.4	400
M_5	VC	AO-240-350	Bo	High	–	2.4	400
M_6	VC and SD	BO-360-120-120	Bi	High	3.6	–	200 (100/100)
M_7	VC	BO-360-075-075	Bi	Low	3.6	–	100 (50/50)
M_8	VC, and SD	EO-240-100-240	Co	High	2.4	–	100
M_9	VC	EO-240-060-240	Co	Low	2.4	–	50

Footnotes:  $b_C$  and  $b_E$  are the dimension parameters of the experimental setups, shown in Figure 4.  $N$  is the total number of participants.  $N_L$  and  $N_R$  are the number of participants entering into the corridor from a waiting area in its left and right sides respectively.

### 3.2.1. Model calibration

Based on the multiobjective calibration framework in [47–49], the three key parameters of the proposed model are calibrated by using the GA (see Table 1). According to prior simulations, the initial range of each parameter is set as follows:  $F_{SN} \in [2, 8]$ ,  $F_{AF} \in [0, 2]$  and  $F_{DF} \in [0, 25]$ .

For the purpose of calibration and crowd movement validation, three types of common motion base scenarios, i.e., a bottleneck flow, a bidirectional flow and a unidirectional corner flow, are used, as shown in Fig. 4. Accordingly, a total of 9 experiments are selected from the data-base of HERMES project [50], shown in Table 2. Considering the computational burden of the parameter optimization, only a high density variant of each scenario is used for calibration according to the suggestion in [47], i.e., a total of three experiments, see Table 2. It should be noted that only the data during the period when the pedestrian density is at the desired level are measured for calibration and validation. For the measurement period, the reader is referred to [51]. To ensure a similar initial condition between simulations and experiments, the flow pattern over time in bidirectional and unidirectional corner flows is extracted from the trajectory data and fed into the model [47]. Moreover, the dynamic floor field is only activated in the bidirectional flow scenario (i.e.,  $F_{DF} = 0$  in other scenarios).

To comprehensively assess each parameter set, three movement metrics (two macro-level metrics: the flow rate (FR) and the density distribution (DD), one meso-level metric: the travel time distribution (TTD)) [47] and one self-organized phenomenon metric (one macro-level metric: average order parameter (AOP)) [52] are used. Microscopic metrics, i.e., trajectories, are not chosen for three reasons. First, a calibration using microscopic metrics requires a different approach (e.g., [53]), not compatible with approaches (e.g., [47]) used for calibrating based on macroscopic and mesoscopic metrics [47]. Second, as suggested in [54], a model calibrated using microscopic metrics does not necessarily produce accurate predictions at the macroscopic and mesoscopic levels. Third, pedestrian simulation models are mostly used to estimate the macroscopic and mesoscopic properties of the infrastructure [55].

**Flow rate (FR).** it is the average flow rate (in p/s/m) of passing a predefined cross-section (see Fig. 4) during the measurement period.

**Density distribution (DD).** the density of each cell is defined as the time (in percentage) it is occupied during the measurement period.

**Travel time distribution (TTD).** it is the distribution (described by the mean ( $\mu_{\text{MT}}$ ) and the standard deviation ( $\sigma_{\text{MT}}$ )) of the time (in s) taken by a pedestrian to traverse the measurement area.

**Average order parameter (AOP).** it is a parameter quantifying lane formation, which is only available in the bidirectional flow scenario, defined in Equation (10) [42].

$$\Phi_{\text{OP}} = \frac{1}{T_{\text{OP}}} \sum_{t=1}^{T_{\text{OP}}} \varphi_{\text{OP}}^t \quad (10)$$

With

$$\varphi_{\text{OP}}^t = \frac{1}{N_{\text{OP}}^t} \sum_{n=1}^{N_{\text{OP}}^t} \phi_{\text{OP}}^{t,i} \quad (11)$$

$$\phi_{\text{OP}}^{t,i} = \frac{\left( N_{\text{OP},\text{same}}^{t,i} - N_{\text{OP},\text{diff}}^{t,i} \right)^2}{\left( N_{\text{OP},\text{same}}^{t,i} + N_{\text{OP},\text{diff}}^{t,i} \right)^2} \in [0, 1] \quad (12)$$

Where  $T_{\text{OP}}$  is the measurement duration (in s);  $\varphi_{\text{OP}}^t$  is an instantaneous order parameter that indicates how pronounced lanes are formed at  $t$ ;  $N_{\text{OP}}^t$  is the number of pedestrians in the measurement area at  $t$ ;  $N_{\text{OP},\text{same}}^{t,i}$  is the number of pedestrians who have the same exit as pedestrian  $i$  and move in  $i$ 's lane at  $t$ , and  $N_{\text{OP},\text{diff}}^{t,i}$  is the number of pedestrians who have a different exit as pedestrian  $i$  and move in  $i$ 's lane at  $t$ , as defined in Eqs. (13)–(14).

$$N_{\text{OP},\text{same}}^{t,i} = \left\{ j, |y^i - y^j| \leq n \text{ and } \vec{D}_P^i \cdot \vec{D}_P^j > 0 \right\} \quad (13)$$

$$N_{\text{OP},\text{diff}}^{t,i} = \left\{ j, |y^i - y^j| \leq n \text{ and } \vec{D}_P^i \cdot \vec{D}_P^j < 0 \right\} \quad (14)$$

For a given metric and setup, the normalized squared error between the simulated and observed values is used to assess the model performance, shown in Equations (15)–(16) [47].

$$\text{dist}_{M,\text{ma}} = \frac{1}{N_M^2} \sum_{k=1}^{N_M^2} \left( \frac{\sum_{q=1}^{N_M^1} M_{\text{sim}}^{k,q} / N_M^1 - M_{\text{exp}}^k}{M_{\text{norm}}^k} \right)^2 \quad (15)$$

$$\text{dist}_{M,\text{me}} = \frac{1}{2} \cdot \left( \frac{M_{\text{sim},\mu} - M_{\text{exp},\mu}}{M_{\text{norm},\mu}} \right)^2 + \frac{1}{2} \cdot \left( \frac{M_{\text{sim},\sigma} - M_{\text{exp},\sigma}}{M_{\text{norm},\sigma}} \right)^2 \quad (16)$$

Where  $\text{dist}_{M,\text{ma}}$  and  $\text{dist}_{M,\text{me}}$  respectively correspond to the normalized squared error related to the macroscopic and mesoscopic metrics.  $N_M^1$  is the number of simulations;  $N_M^2$  is the number of travel directions for the FR, the number of cells for the DD, and 1 for the AOP;  $M_{\text{sim}}$  and  $M_{\text{exp}}$  are, respectively, the simulated and observed values for a given metric;  $M_{\text{norm}}$  is the normalization value (for more details, the reader is referred to [49]).

A set of metrics and setups used in the calibration procedure generates multiple objective functions, which are combined as a single objective function in Eq. (17) using the weighted sum method [11]. Thus,  $\text{dist}_M$  is the optimization objective of the GA.

$$\text{dist}_M = \frac{3}{4} \cdot \left( \frac{1}{N_M^3 N_M^4} \sum_{i=1}^{N_M^3} \sum_{j=1}^{N_M^4} \text{dist}_M^{i,j} \right) + \frac{1}{4} \cdot \text{dist}_{M,\Phi_{\text{op}}} \quad (17)$$

Where  $N_M^3$  and  $N_M^4$  respectively correspond to the number of setups and movement metrics;  $\text{dist}_M^{i,j}$  is the normalized squared error between the simulated and observed values of movement metric  $j$  in setup  $i$ ;  $\text{dist}_{M,\Phi_{\text{op}}}$  is the normalized squared error between simulated and observed values of  $\Phi_{\text{op}}$ .

### 3.2.2. Model validation and comparison

This section introduces the individual and crowd movement simulation setups used in the model validation and the performance comparison with the counterpart model.

**3.2.2.1. Individual movement.** The main objective of the case studies related to individual movement is to validate the capability of our model to resolve the diagonal movement artefact [12] in the existing CA models, and to show its performance advantage over Fu et al.'s model [7]. The physical setups shown in Fig. 3 are chosen as the simulation scenarios. At each simulation run, the **movement trajectory** is recorded.

**Table 3**

Overview of the simulation setups, where the acronyms identify the simulation types (SC = static floor field construction, IM = individual movement, and CM = crowd movement).

Tested algorithm/model/effect	Scenario setups	Simulation types	Used model	Comparison base	Counterpart algorithm/model	Metrics
SFF-Construction (question 1)	S_1, S_2	SC	Model in Kirchner and Schadschneider [14]	The exact algorithm [13]	The existing approximate algorithms [14,17]	AE
		IM			TMT, trajectory	TET, MIET
		CM				
LM-Determination (question 2)	S_1, S_2	IM	<b>LM-Determination</b>	The ideal result	Fu et al.'s model [7]	Trajectory
	M_4- M_9 [50]	CM		Empirical data		FR, DD, TTD, AOP
Discretization effect (question 3)	S_1, S_2	IM	<b>LM-Determination</b> and Fu et al.'s model [7]	-	-	TMT, trajectory
	M_4, M_6, M_8 [50]	CM		-	-	MIET, FR, DD, AOP

**3.2.2.2. Crowd movement.** In terms of crowd movement, the main objective of the case studies is to validate the capability of our model to reproduce the locomotion behaviour observed empirically (including locomotion movement and self-organized lane formation), and to evidence its performance advantage over the model of Fu et al. [7].

To make a comprehensive assessment for the model performance in different density scenarios, both the high and low density variants of each scenario except the bottleneck flow scenario which only has a high density variant are used (i.e., six experiments), see Table 2. Similar to the calibration procedures, four metrics (i.e., FR, DD, TTD, AOP) are measured for the specific setup in experiments and simulations, and the model performance for a given metric and setup is assessed by the normalized squared error in Eqs. (15) and (16).

The parameter values of Fu et al.'s model are determined by the procedures in Appendix C. It should be noted that the simulations related to the bidirectional flow scenario (i.e., setups M\_2 and M\_6) will not be conducted for Fu et al.'s model, as indicated in Appendix C.

### 3.3. Part 3: Discretization effect

After calibration and validation, the discretization effect on the individual and crowd movement simulation is investigated by the comparative simulation analyses using our and Fu et al.'s models. It is worth noting that the movement velocity rule and the update rule are the same in these two models, which lays a sound base for the analyses.

#### 3.3.1. Individual movement

To elucidate how the discretization degree influences the performance of CA models in simulating individual movement, simulation analyses are conducted by using the setups and movement metrics in Section 3.2.2.1.

#### 3.3.2. Crowd movement

To illuminate how the discretization degree impacts the outcomes of the crowd movement simulation in CA models, setups M\_4, M\_6 and M\_8 are taken as the illustrative examples for simulation analyses (one experiment for each motion base scenario), see Table 2. It should be noted that the whole evacuation process from each setup is simulated, which is slightly different from the calibration and validation procedures. Four metrics are measured at each simulation run, i.e., the **mean of individual evacuation times (MIET)**, the **flow rate (FR)**, the **density distribution (DD)**, and the **Average order parameter (AOP)**.

### 3.4. Summary

The simulation setups are summarized in Table 3.

## 4. Results

The results of the three parts of simulation analyses are respectively presented in Sections 4.1–4.3.

#### 4.1. Part 1: SFF construction algorithm

The calibrated value of  $\alpha_{SF}$  that obtains the minimum error ( $dist_{SF}$ ) is 1.074, which will be used in this paper. This section presents the results of the comparison between the proposed SFF approximate algorithm and the existing SFF approximate algorithms.

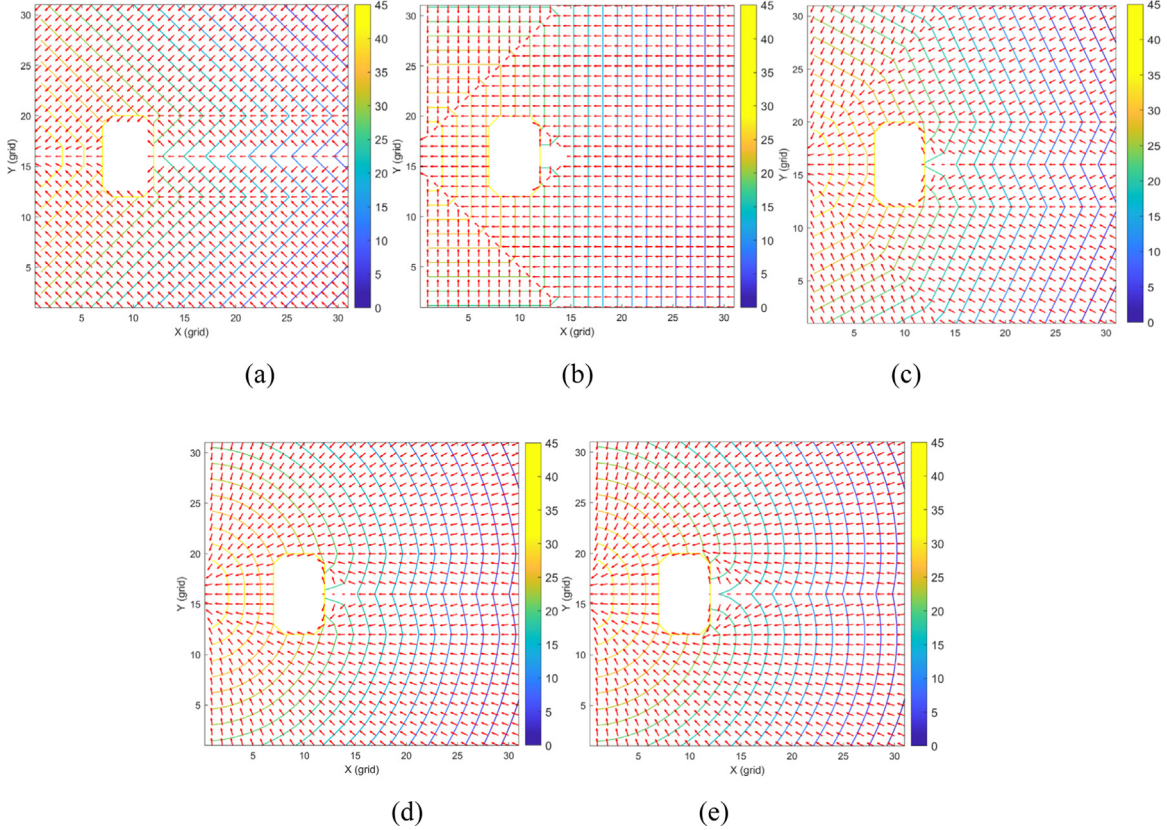


**Fig. 5.** Contour map (the colour of the contour lines changes from dark blue to dark yellow as the SFF value increases) and the gradient directions (denoted by red arrows) of the static floor fields in setup S\_2, constructed by different algorithms. (a): Approximate algorithm in Kirchner and Schadschneider [14] (Neumann neighbourhood), (b): Approximate algorithm in Kirchner and Schadschneider [14] (Moore neighbourhood), (c): Approximate algorithm in Huang and Guo [17] ( $\varepsilon = 0.5$ ), (d): Approximate algorithm in this paper ( $\alpha_{sf} = 1.074$ ), (e): Exact algorithm in Nishinari, et al. [13].

#### 4.1.1. SFF computation accuracy comparison

Since the algorithm performance is essentially independent of the physical setups, the results of the more complicated geometry (setup S\_2) are visualized, shown in Fig. 5. It can be seen that the static floor fields constructed by the existing approximate algorithms (Fig. 5(a), (b) and (c)) are significantly non-isotropic, whereas our algorithm generates an approximately isotropic SFF (Fig. 5(d)), which is awfully close to that of the exact algorithm (Fig. 5(e)). It can be found that in the non-isotropic SFF, the gradient direction of most lattice sites points towards a transverse line perpendicular to the exit or a  $45^\circ$  diagonal line rather than the exit cells or the shortest path leading to the exit, which will lead to the diagonal movement of pedestrians in CA models. However, this phenomenon disappears in our SFF, ascribed to the accurate approximation of the shortest distance.

As presented in Table 4, the proposed approximate algorithm obtains a significantly lower absolute error (AE) than the state-of-the-art approximate algorithms when compared with the exact algorithm. The results quantitatively demonstrate the prominent computation accuracy advantage of our algorithm in the scenarios with and without obstacles, which complements the proof in Appendix B.

#### 4.1.2. Individual movement simulation accuracy comparison

As presented in Fig. 6, it is clearly observed that in the static floor fields constructed by the existing three approximate algorithms [14–17], the pedestrian moves along a transverse line perpendicular to the exit or a  $45^\circ$  diagonal line, leading to unrealistically diagonal movement trajectories and a statistically significant increase or decrease in the movement time (based on  $t$ -tests) as compared to the results of the exact algorithm [13]. These results are consistent with the finding of Nishinari, et al. [13] and Pelechano and Malkawi [12], who observed the diagonal movement of pedestrians when the Neumann neighbourhood algorithm [14] is used to construct the SFF. Expectedly, our algorithm obtains the trajectories that are almost overlapped with that of the exact algorithm and nearly the same movement time (with no statistically significant difference). Moreover, it can be seen that there is still a prominent discrepancy between the ideal trajectory (i.e., the trajectory without the diagonal movement artefact) and that of the exact algorithm [13]. This should be ascribed to the insufficiently realistic behavioural rules of the used model (i.e., the model in [14]), as indicated in Section 4.2.2.1.

**Table 4**

The descriptive statistics of AE for different approximate algorithms in setups S\_1 and S\_2, where that of our algorithm are in bold.

Algorithms	Mean		Min.		Max.		S.D.	
	S_1	S_2	S_1	S_2	S_1	S_2	S_1	S_2
Kirchner and Schadschneider [14] (Neumann neighbourhood)	6.57	6.00	0	0	10.99	10.98	8.84	6.54
Kirchner and Schadschneider [14] (Moore neighbourhood)	1.90	1.67	0	0	3.01	3.02	0.93	0.681
Huang and Guo [17]	2.47	2.31	0	0	3.99	3.98	1.02	0.80
<b>Ours</b>	<b>0.01</b>	<b>0.10</b>	<b>0</b>	<b>0</b>	<b>0.03</b>	<b>1.08</b>	<b>0.01</b>	<b>0.18</b>

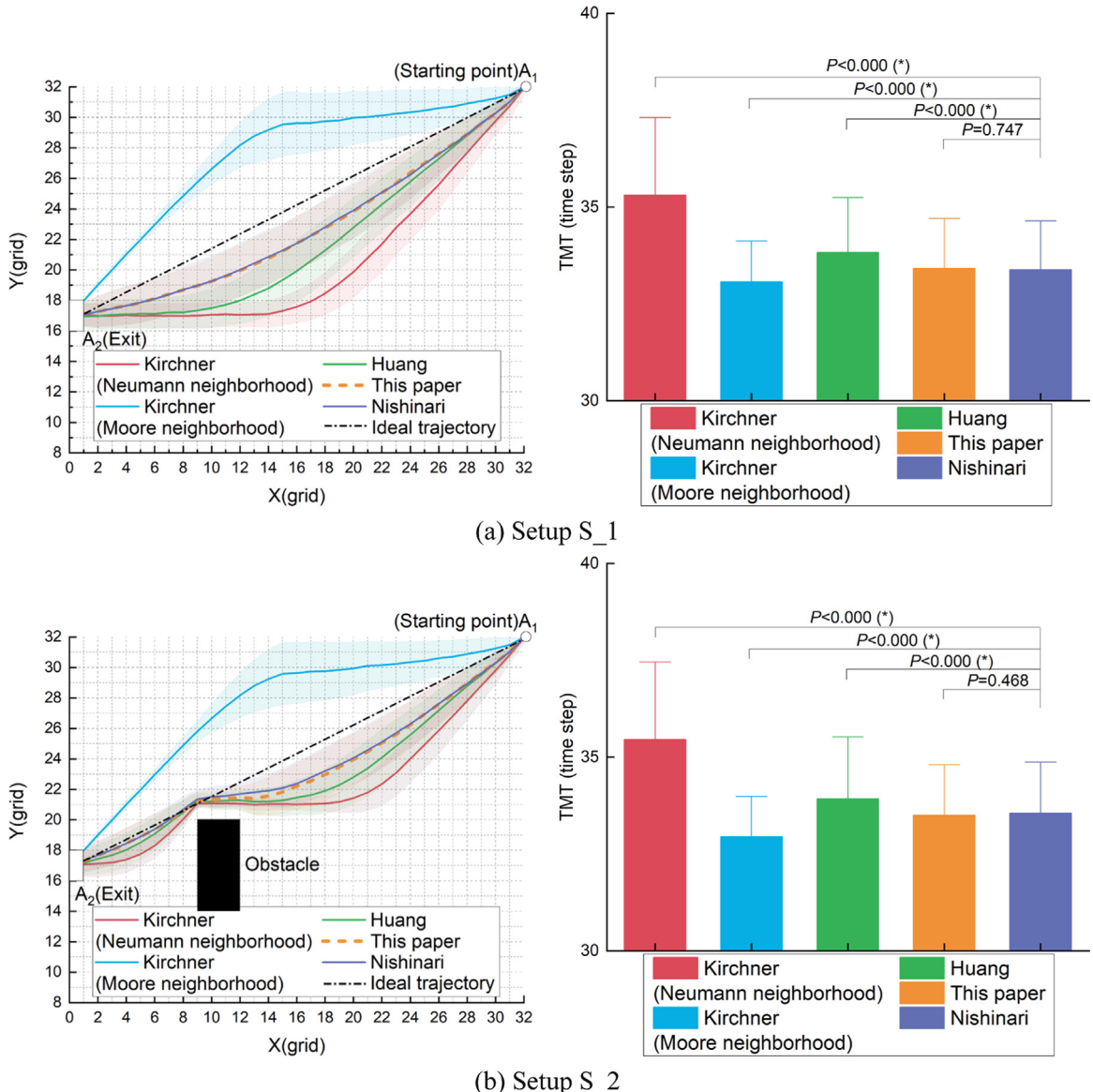


**Fig. 6.** Comparisons of the individual movement results derived from using different SFF algorithms in setups S\_1 and S\_2. The plots on the left show the average (lines) and the standard deviations (error bands) of the trajectories, where the ideal trajectory (i.e., the trajectory without the diagonal movement artefact) is also presented and each grid represents R m × R m. The plots on the right show the average and the standard deviations of the total movement times (TMT), and the asterisk sign (\*) indicates the difference is statistically significant at 99% level by t-test.

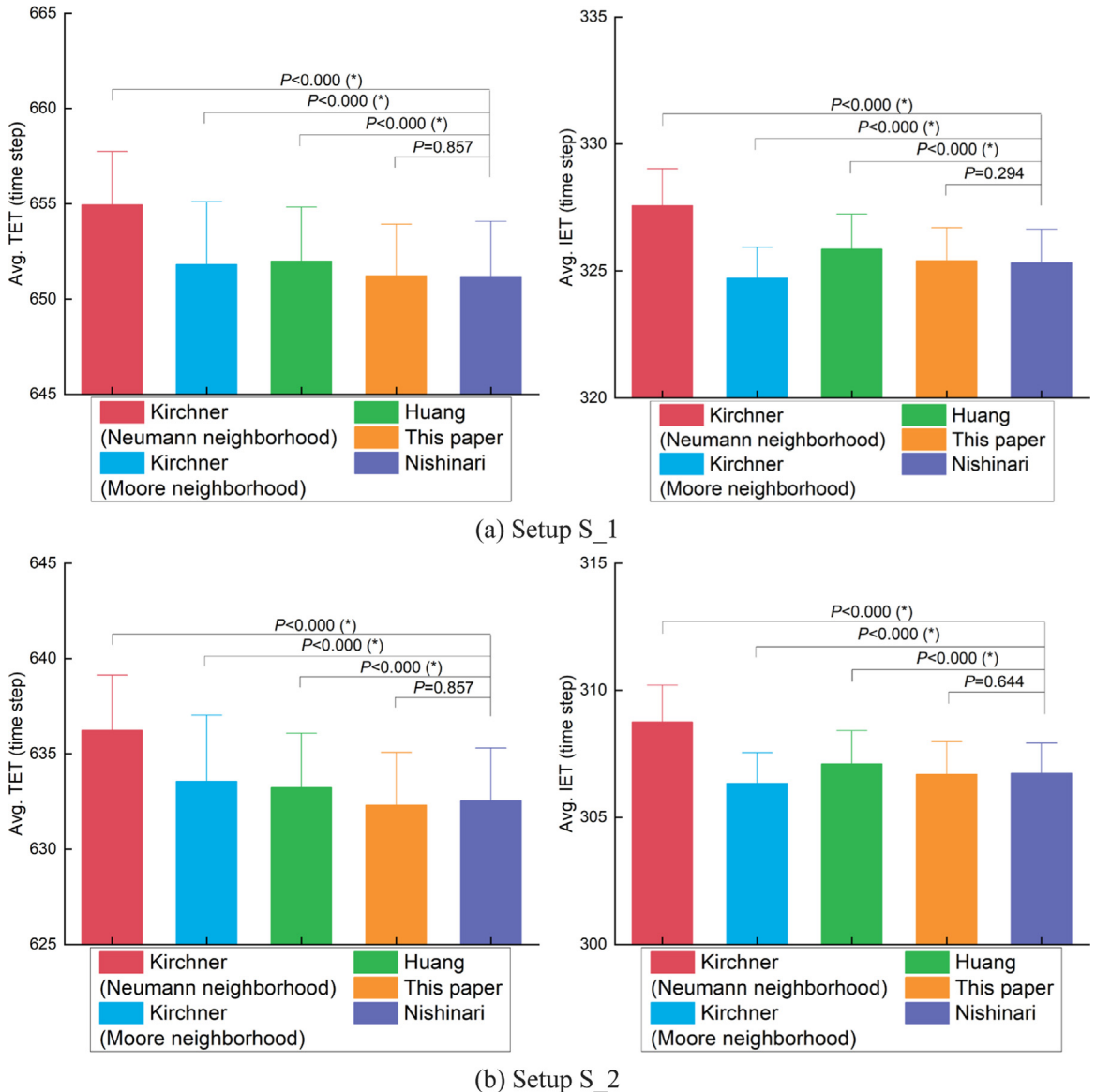


**Fig. 7.** Comparisons of the crowd evacuation results derived from using different SFF algorithms in setups S\_1 and S\_2. The plots on the left show the average and the standard deviations of the total evacuation times (TET). The plots on the right show the average and the standard deviations of the individual evacuation times (IET), and the asterisk sign (\*) indicates the difference is statistically significant at 99% level by *t*-test.

#### 4.1.3. Crowd evacuation simulation accuracy comparison

As presented in Fig. 7, the total and individual evacuation times of the existing three approximate algorithms [14,17] are significantly longer or shorter than the exact algorithm [13], whereas the difference between the results of our algorithm and the exact algorithm is not statistically significant. As aforementioned, this should be ascribed to the non-isotropy of the static floor fields constructed by the existing approximate algorithms [14,17], which gives rise to the diagonal movement of pedestrians in simulations.

#### 4.2. Part 2: Locomotion movement model

In this section, the calibration and validation results of the proposed locomotion movement model are presented.

##### 4.2.1. Model calibration

Table 5 shows the parameter set with the best fitness for our model. The calibrated static field sensitivity parameter value of Fu et al.'s model is 1.7 (*NB*: in Fu, et al. [7], the value is 2 or 0.8). The simulation errors of our and Fu et al.'s models

**Table 5**  
Calibrated parameter values of our model.

Parameter	$F_{SN}$	$F_{AF}$	$F_{DF}$
Value	4.08	16	1.2

**Table 6**

Calibration results of our and Fu et al.'s models, where the acronyms identify the metrics (i.e., FR = Flow rate, DD = density distribution, TTD = travel time distribution, AOP = average order parameter) and the scenarios (i.e., Bi = bidirectional, Bo = Bottleneck, and Co = Corner).

Model	Setup	FR	DD	TTD	AOP	Weighted sum ( $dist_M$ )
Ours	M_1 (Bo)	0	0.329	0.163	–	0.184
	M_2 (Bi)	0.002	0.340	0.098	0.074	
	M_3 (Co)	0	1.021	0.038	–	
Fu et al.	M_1 (Bo)	0.134	0.565	0.004	–	0.570
	M_2 (Bi)	–	–	–	–	
	M_3 (Co)	0.089	2.115	0.514	–	

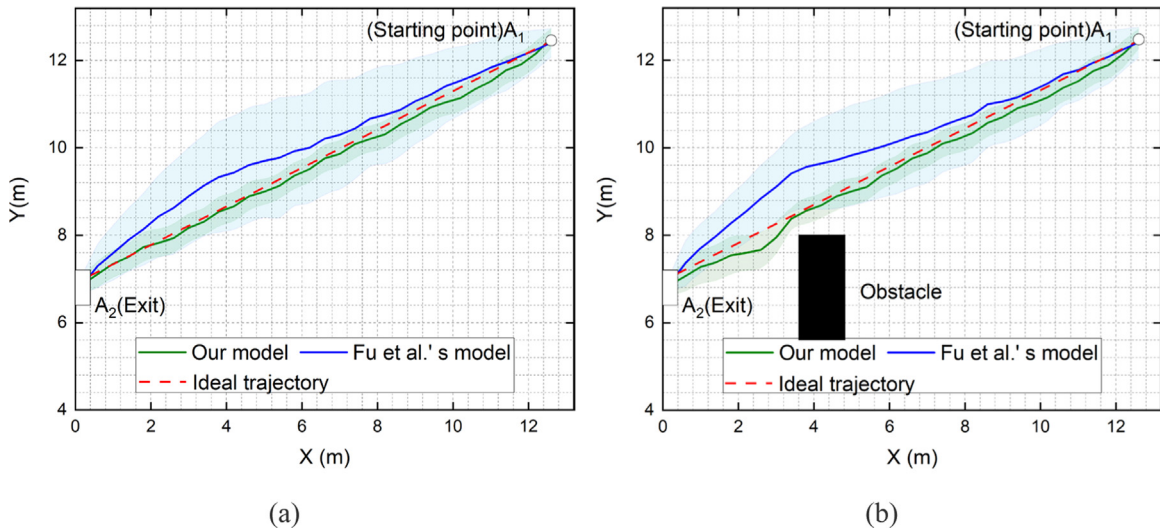


**Fig. 8.** Individual movement trajectory comparisons between our and Fu et al.'s models in setups S\_1 and S\_2. The plots (a) and (b) show the average (lines) and the standard deviations (error bands) of the trajectories, where the ideal trajectory is also presented and each grid represents  $R \text{ m} \times R \text{ m}$ .

with the calibrated parameter values are shown in Table 6. It can be seen that except the DD (density distribution) the errors of other metrics are small in both models, which justifies the calibrated parameter values. As suggested in Sparnaaij, et al. [47], the relatively large errors in the DD could be ascribed to the difference in the boundary conditions between experiments and simulations (e.g., the sequence of pedestrians entering into the physical setup) due to the lack of related experimental information, which would negatively impact the models' capability to fit the empirical data.

#### 4.2.2. Model validation and comparison

**4.2.2.1. Individual movement.** Fig. 8 shows the individual movement trajectories obtained from our and Fu et al.'s models in setups S\_1 and S\_2. The unrealistically diagonal movement trajectories can be clearly observed in Fu et al.'s model, whereas our model's trajectories are nearly overlapped with the ideal one. Moreover, the variation of the trajectories in Fu et al.'s model is significantly larger than our model. The results demonstrate that the proposed model can resolve the diagonal movement artefact [12,13] of the existing CA models.

It should be noted that the SFF approximate construction algorithm of Huang and Guo [17] is used in Fu et al.'s model [7]. Thus, according to these results and those in Section 4.1.2, it can be found that two factors contribute to the diagonal movement artefact, i.e., the non-isotropic SFF, and the insufficiently realistic behavioural rules of the model (i.e., the model realism).

**4.2.2.2. Crowd movement.** Table 7 presents the prediction errors of our and Fu et al.'s models when compared with experiments. It can be seen that in our model, the error between the simulated and observed values of the FR is close to

**Table 7**

Prediction errors of our and Fu et al.'s models in the crowd movement simulation, where the acronyms identify the metrics (i.e., FR = Flow rate, DD = density distribution, TTD = travel time distribution, AOP=average order parameter) and the scenarios (i.e., Bi = bidirectional, Bo = Bottleneck, and Co = Corner).

Setup	Model	FR	DD	TTD	AOP
M_4 (Bo)	Ours	0	0.549*	0.486	-
	Fu et al.	0.330	0.430*	2.438	-
	Ratio=(Ours-Fu)/Fu	<b>-1.00</b>	<b>0.277*</b>	<b>-0.801</b>	-
M_5 (Bo)	Ours	0.004	1.413*	0.379*	-
	Fu et al.	0.034	1.308*	0.134*	-
	Ratio=(Ours-Fu)/Fu	<b>-0.882</b>	<b>0.080*</b>	<b>1.828 *</b>	-
M_6 (Bi)	Ours	0	0.554	0.021	0.044
M_7 (Bi)	Ours	0.003	0.158	0.055	0.175
M_8 (Co)	Ours	0.003	0.255	0.029	-
	Fu et al.	0.030	1.372	0.724	-
	Ratio=(Ours-Fu)/Fu	<b>-0.900</b>	<b>-0.814</b>	<b>-0.960</b>	-
M_9 (Co)	Ours	0.001	0.010	0.004	-
	Fu et al.	0.008	0.600	1.292	-
	Ratio=(Ours-Fu)/Fu	<b>-0.875</b>	<b>-0.983</b>	<b>-0.997</b>	-

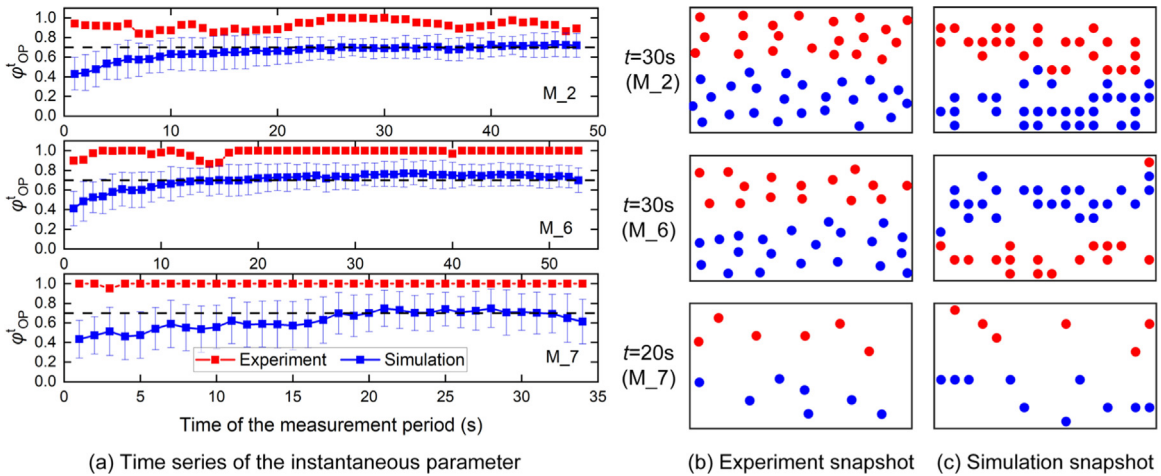


**Fig. 9.** Results related to lane formation in experiments and simulations for setups M\_2, M\_6 and M\_7. The blue circles in plots (b) and (c) denote the pedestrians moving from the left to the right. The black dotted lines in plot (a) indicate  $\varphi_{\text{OP}}^t = 0.7$ .

zero for all setups. In terms of the DD and TTD, a rather low error value is also observed for setups M\_6, M\_7, M\_8 and M\_9. These results suggest that the proposed model is capable of replicating the crowd movement behaviour empirically observed in bottleneck, bidirectional and corner flows. Moreover, it can be clearly observed that the results of our model are superior to those of Fu et al.' model except the three cases (i.e., DD in M\_4, DD and TTD in M\_5). To make a quantitative comparison, the relative error between the two models for each metric is also provided in Table 7. It can be found that the errors of our model are reduced by 50.2% on average in comparison to the model of Fu et al. This means that the results of our model are closer to that of experiments.

To better visualize the ability of our model to reproduce the lane formation phenomenon, Fig. 9(a) shows the experimental and simulated time series of the instantaneous order parameter ( $\varphi_{\text{OP}}^t$ ) in the measurement period. The closer  $\varphi_{\text{OP}}^t$  is to 1, the more pronounced the self-organized lane formation is. It can be seen that the simulated  $\varphi_{\text{OP}}^t$  increases to a stable value not less than 0.7 after a warm-up stage in the three setups. The steady density in the measurement area is respectively around 2.5, 2.0 and 0.7 per/m<sup>2</sup> in setups M\_2, M\_6 and M\_7. Although the simulated  $\varphi_{\text{OP}}^t$  is slightly smaller than that of experiments, two stable self-organized lanes are clearly observed in both simulations and experiments, as shown in Fig. 9(b) and (c). The results prove that our model is able to reproduce lane formation in different density situations. Moreover, under the density condition of 2.0 per/m<sup>2</sup>, the value of  $\varphi_{\text{OP}}^t$  in Tordeux et al.'s model [56] and Xu et al.'s model [57] is respectively constantly lower than 0.3 and 0.7 (as indicated in [52] (Fig. 11)), whereas the average value of  $\varphi_{\text{OP}}^t$  in the stable stage (10 s–53 s in setup M\_6) in our model is 0.73. This means that our model reproduces lane formation much better than Tordeux et al.'s model [56] and Xu et al.'s model [57] in the same density condition. The remaining discrepancy between the experimental and simulated  $\varphi_{\text{OP}}^t$  should be ascribed to the difference in the structure of lanes in simulations and experiments (see Fig. 9(b) and (c)).

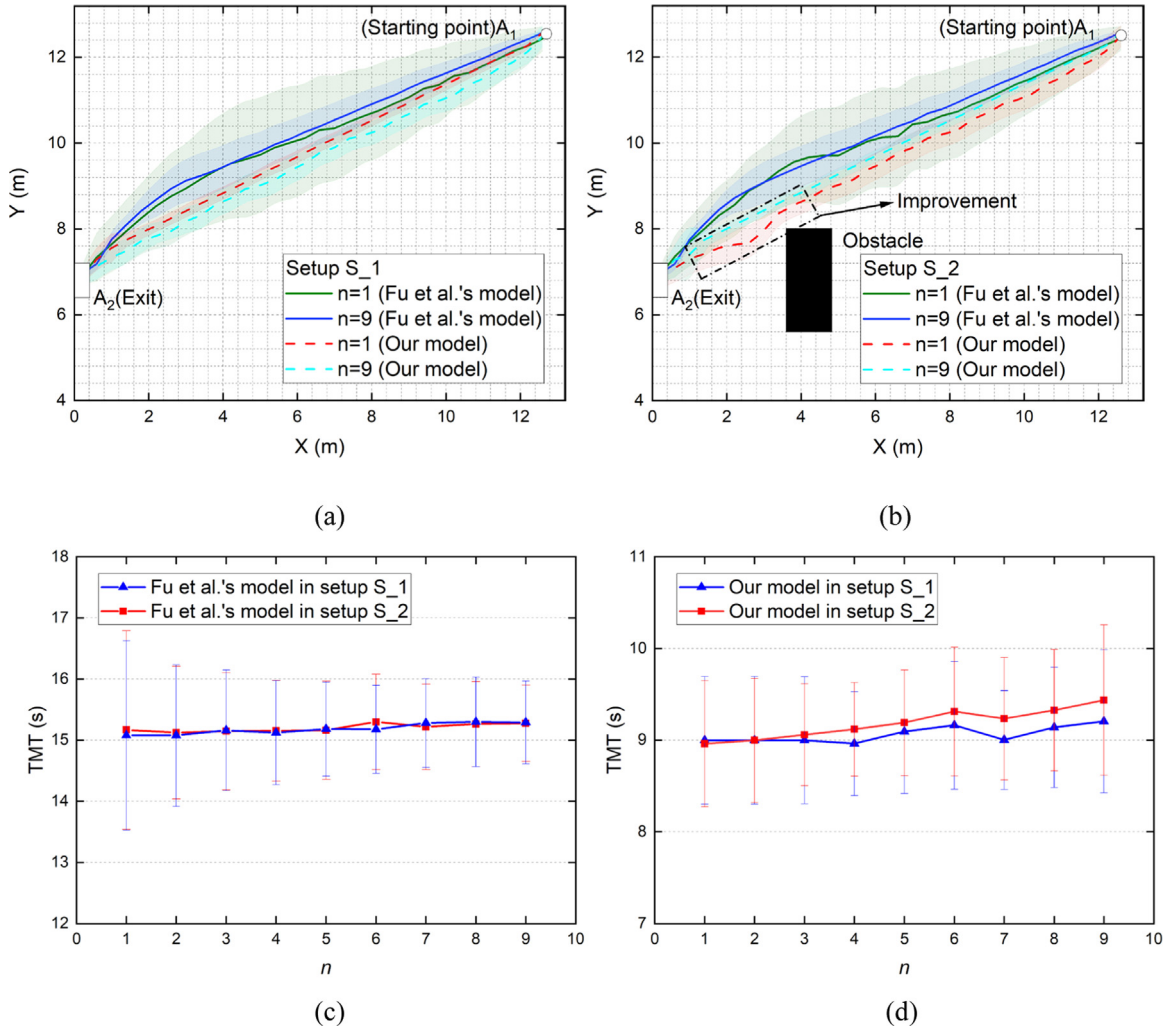


**Fig. 10.** Effect of the discretization degree ( $n$ ) on individual movement simulation outcomes in our and Fu et al.'s models in setups S<sub>1</sub> and S<sub>2</sub>. The plots (a) and (b) show the average (dashed and solid lines) and the standard deviations (error bands) of the trajectories, where each grid represents  $R \text{ m} \times R \text{ m}$ . The plots (c) and (d) show the total movement time (TMT) against the discretization degree.

#### 4.3. Part 3: Discretization effect

In this section, the discretization effect in CA models is revisited to shed fresh light on its common characteristics and the underlying reasons by comparative analyses using our and Fu et al.'s models.

##### 4.3.1. Individual movement

Fig. 10 shows the effect of the discretization degree on the individual movement trajectory and time in our and Fu et al.'s models. In Fig. 10(a) and (b), only the results when the discretization degree  $n=1$  and 9 are presented so as to clearly show the change in the movement trajectories. It can be found that finer discretization cannot alleviate the diagonal movement artefact in the model of Fu et al. which also demonstrates the findings in Section 4.2.2.1, see Fig. 10(a). However, one can see that in our model, finer discretization further improves the movement trajectories in setup S<sub>2</sub>, as illustrated in Fig. 10(b). As for the individual movement time, it slightly increases with the discretization degree in setups S<sub>1</sub> and S<sub>2</sub> for both models, see Fig. 10(c) and (d). Moreover, it can be found that finer discretization reduces the variation of the movement trajectories and times, which is more prominent in Fu et al.'s model than our model. As suggested in Xu, et al. [30], these changes should be ascribed to the more accurate individual movement due to finer discretization, leading to more realistic and less variable results. These results suggest that the discretization degree has a significant impact on the individual movement simulation, which varies depending on the used model.

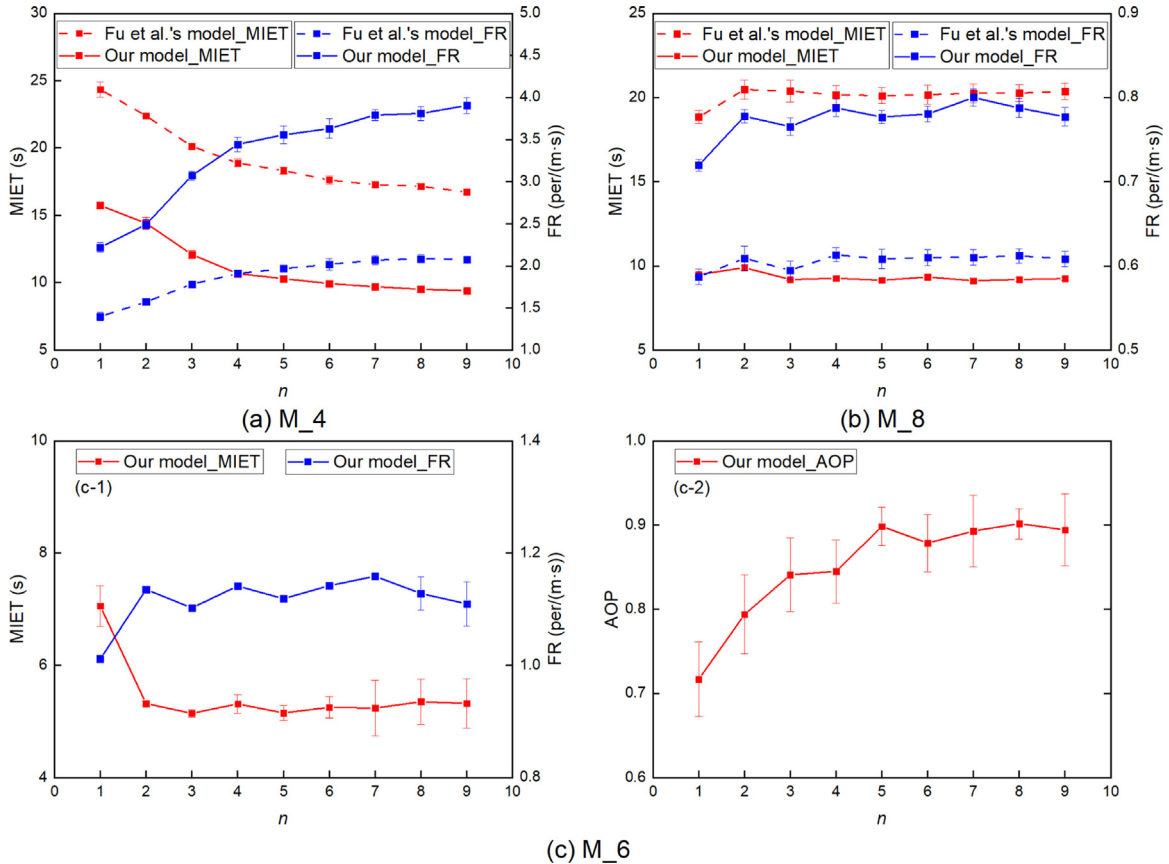


**Fig. 11.** Effect of the discretization degree ( $n$ ) on the mean of individual evacuation times (MIET), the flow rate (FR) and the average order parameter (AOP) in setups M\_4, M\_6 and M\_8 for our and Fu et al.'s models.

#### 4.3.2. Crowd movement

Fig. 11 presents the effect of the discretization degree on the mean of individual evacuation times (MIET), the flow rate (FR) and the average order parameter (AOP) in setups M\_4, M\_6 and M\_8. For each setup, the density distribution (DD) with the discretization degree  $n = 1, 5$  and 9 is exemplified in Fig. 12 to illustrate the discretization effect. One can see that except the MIET in setup M\_8, a similar discretization effect is observed in our and Fu et al.'s models. This suggests the generalizability of our findings, which are summarized as follows.

(1) The FR invariably increases as the discretization degree increases from  $n = 1$  to  $n = 2$  in setups M\_4, M\_6 and M\_8, shown in Fig. 11(a), (b) and (c).

(2) As the discretization degree continues to increase, the FR of setups M\_6 and M\_8 fluctuates around certain values, while that of setup M\_4 maintains the increasing trend, shown in Fig. 11(a), (b) and (c).

(3) In terms of the MIET, a variation trend opposite to that of the FR is observed in all setups except M\_8, shown in Fig. 11(a), (b) and (c).

(4) The degree of spatial discretization influences the pedestrian distribution in evacuations, shown in Fig. 12.

(5) Finer discretization facilitates the formation of lanes in setup M\_6, and such a promoting effect vanishes when the discretization degree increases to exceed a certain value, shown in Fig. 11(c) and Fig. 12(e).

The first four observations are by-and-large consistent with those of Guo [31] who found that the total evacuation time of pedestrians in a square room with an exit decreases when the discretization degree increases from  $n = 1$  to  $n = 9$ , and that the crowd shape near the exit is affected by the discretization degree. However, the first three observations are quite different from that of Fu et al. [7], in which they found that in a square room with one exit, finer discretization first increases the average evacuation time, and then such a negative effect vanishes when the discretization degree  $n \geq 3$ . Similarly, Xu, et al. [30] also observed the negative effect of spatial discretization on the evacuation times.

To identify the underlying reasons for the discrepancy between the observations regarding the evacuation efficiency, the discretization effect in the setup used in Fu et al. [7] (denoted as F\_1) and another similar setup designed for comparison (denoted as F\_2) is investigated by using our and Fu et al.'s models (See Appendix D). The results in Fig. 11 and D.1 suggest that the discretization degree actually has a double-side effect on the evacuation efficiency. One

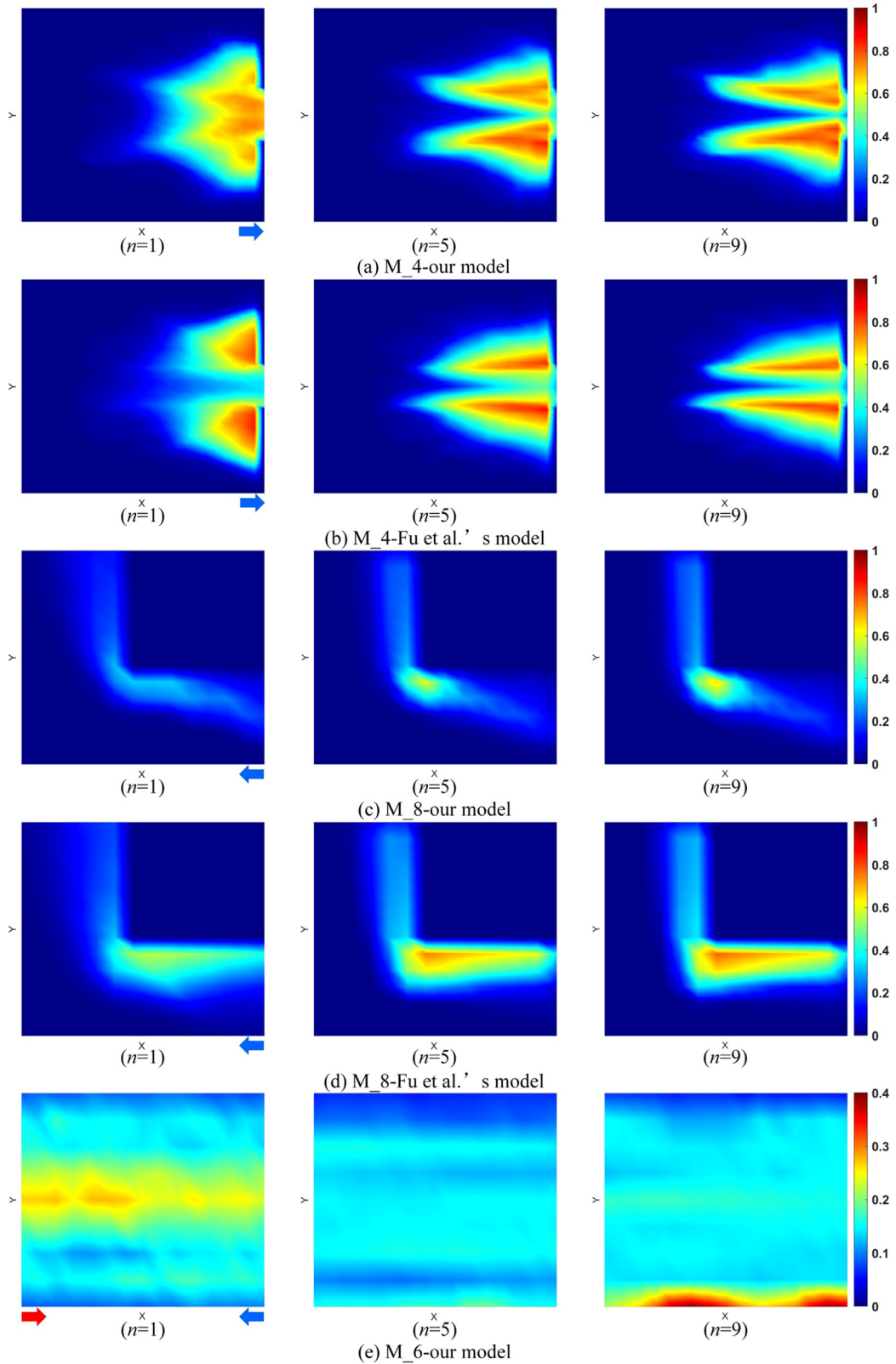


**Fig. 12.** The density distribution (DD) map in setups M4, M6 and M\_8 with the discretization degree  $n = 1, 5$  and 9. The colour changes from dark blue to dark red as density increases. The blue and red arrows in the left column plots indicate the flow direction of each setup.

possible explanation is as follows. On one hand, finer discretization leads to more frequent conflicts and thus reduces the evacuation efficiency, as suggested in [30]. On the other hand, a higher degree of spatial discretization makes it more difficult for pedestrians to change the movement lane and overtake others ahead, and thus facilitates the formation of orderly movement queues (demonstrated by the fifth finding and the observation in [30]). The influence of the discretization degree on the evacuation efficiency in the specific scenario is mainly a result of the joint effect of these two factors. The latter reduces the movement stagnation due to lane changes and thus is never detrimental to the evacuation efficiency of pedestrians [30]. Thus, the increase of the evacuation efficiency in setups M\_4, M\_6, M\_8 and F\_2 should be ascribed to the formation of movement queues. However, its positive effect is rather weak in the scenarios with a narrow exit due to the restricted outflow (e.g., setup F\_1). And, the negative effect of conflicts among pedestrians is prominent in the situations where pedestrians are randomly distributed due to dislocation (e.g., setup F\_1). These results suggest that the discretization effect is closely related to the geometric structures (e.g., setups M\_4 vs. F\_1) and the pedestrian distribution (e.g., setups F\_1 vs. F\_2).

Moreover, with the discretization degree  $n = 2$ , a relatively stable movement order among pedestrians can be formed when they enter into setups M\_6 and M\_8. Correspondingly, the FR first increases as the discretization degree changes from  $n = 1$  to  $n = 2$ , and then remains relatively constant, irrespective of  $n$ . However, in setup M\_8, the MIET is nearly unchanged in our model and slightly increases in Fu et al.'s model, which is inconsistent with the variation of the FR. It should be noted that compared with the FR, the MIET can more acutely capture the change in the individual evacuation efficiency since the MIET and FR are respectively macroscopic and mesoscopic metrics. The density distribution map in Fig. 12(c) and (d) reveals the potential reason for the change of the MIET in setup M\_8. It can be seen that finer discretization aggravates the formation of high-density zones before the corner [58], and this phenomenon is more prominent in Fu et al.'s model than our model. This is because finer discretization diminishes the movement flexibility of pedestrians, leading to delays in rounding the corner. Thus, the MIET remains relatively constant (in our model) or even increases (in Fu et al.'s model) in setup M\_8. These results suggest that the discretization effect is correlated with the geometric structures (e.g., setups M\_4 and M\_6) and the used simulation model (e.g., our model vs. Fu et al.'s model).

## 5. Conclusions

This work focuses on the three well-known problems in the existing CA models, i.e., the efficient and accurate construction of the SFF, the insufficient simulation accuracy and the discretization effect. To this end, a novel approximate algorithm is proposed to efficiently and accurately construct the SFF, based on which the static navigation field is straightforwardly created by the proposed method, which provides navigation directions for pedestrian locomotion movement. With the introduction of the typical movement behaviour characteristics (including the steering behaviour, the lane-level anticipation and the herding behaviour), a novel fine discrete CA model based on the desired direction is developed to capture the operational-level (locomotion) behaviour. The novel SFF approximate construction algorithm and locomotion movement model are validated and compared to the state-of-the-art approaches from the theoretical and/or numerical perspective(s) in different indoor environments. Thereafter, comparative analyses in various scenarios are conducted by using our model and Fu et al.'s model [7] (the state-of-the-art fine discrete CA model) to systematically elucidate the effect of the discretization degree on the simulation outcomes of individual and crowd movement. The main findings corresponding to the investigated three questions are summarized as follows:

(1) (*question 1*) The results demonstrate the significant accuracy advantage of the proposed SFF approximate construction algorithm over the state-of-the-art SFF approximate construction algorithms [14–17]. With the overwhelming advantage in computation complexity and the excellent approximation performance in computation accuracy, and individual and crowd movement simulation accuracy, our algorithm is a promising way to resolve the dilemma between more sophisticated behaviour simulations by using the exact algorithm [13] and the consequent significant decrease in computational efficiency. The simulations show that the non-isotropic SFF leads to significantly unrealistic and biased results at the microscopic and macroscopic levels.

(2) (*question 2*) The simulation results demonstrate that the proposed locomotion movement model can resolve the diagonal movement artefact [12] of the existing CA models in the individual movement simulation. In terms of the crowd movement simulation, when compared with experiments the results of our model are superior over those of Fu et al.'s model, with a 50.2% improvement in the prediction accuracy. Also, our model is capable of replicating the lane formation phenomenon in different density conditions. With the ability to reproduce the empirical observations in manifold scenarios, the proposed model can serve to study pedestrian evacuation problems.

(3) (*question 3*) The by-and-large consistent discretization effect is observed in our and Fu et al.'s models. It is found that the discretization degree significantly influences the individual and crowd movement simulation outcomes, which is closely related to the used model and the setup of the scenarios (the geometries and the pedestrian distribution). These results systematically clarify the discretization effect in CA models and disclose the underlying reasons for the inconsistent evidence in literature. It is thus recommended that particular care should be taken when the discretization degree of the calibrated and validated CA model has to be changed to satisfy the requirements of practical applications.

In future work, the proposed locomotion movement model should be further examined in more motion base cases (e.g., crossing flows) and density situations. And further development is necessary to allow reproducing more characteristic behaviours observed in real crowds (e.g., group behaviour [38]). Moreover, for practical applications in complex scenarios (e.g., transport vehicles [59]), the model should be extended to incorporate the scenario-dependent rules and encapsulated with the strategic and tactical decision-making modules (e.g., [51]) so as to build a complete simulation package that can capture the behaviour at different levels.

**Table A.1**

Key notation of the SFF algorithm and locomotion movement model.

Notation	Description
SFF algorithm (Algorithm 1. SFF – Construction)	
$\mathbb{C}$	Environmental information of the geometry
$\alpha_{SF}$	Parameter of controlling the computation accuracy
$ST^e$	Set of the cells that can be traversed by pedestrians to evacuate through exit $e$
$SF^e$	Set of the SFF value of all cells to exit $e$
$SD^e$	Set of the distance of all cells to exit $e$
$NF^{e,(i,j)}, MF^{e,(i,j)}, SD^{e,(i,j)}$	Distance of cell $(i,j)$ to exit $e$ , calculated by the Neumann neighbourhood, the Moore neighbourhood and the proposed algorithm respectively
$SF^{e,(i,j)}$	SFF value of cell $(i,j)$ to exit $e$
Locomotion movement model (Algorithm 2. LM-Determination)	
$F_{SN}$	Sensitivity parameter of the static navigation field
$F_{AF}$	Sensitivity parameter of the lane-level anticipation field
$F_{DF}$	Sensitivity parameter of the dynamic floor field
$t$	Cumulative time step of the evacuation
$\vec{D}^{(i,j)}$	Navigation direction of cell $(i,j)$
$\vec{D}_A^q$	Desired direction of pedestrian $q$
$P_S^q$	Steering probability of pedestrian $q$
$v^{q,t}$	Velocity of pedestrian $q$ at $t$
$v_{\max}$	Maximum velocity of the evacuation system of pedestrians
$\vec{D}^k$	Candidate movement direction ( $k = 1, 2, \dots, 8$ , represents eight directions that span anticlockwise from the east, shown in Fig. 2)
$AF^{\vec{D}^k}$	Lane-level anticipation field value of $\vec{D}^k$
$DF^{\vec{D}^k}$	Dynamic floor field value of $\vec{D}^k$
$S_p$	Set of lattice sites that are not occupied by obstacles
$\omega^q$	Pedestrian angular speed, set as $\pi/s$ [51]

## CRediT authorship contribution statement

**Rong Huang:** Conceptualization, Methodology, Model implementation, Analysis and interpretation of results, Reviewed result. **Xuan Zhao:** Conceptualization, Methodology, Analysis and interpretation of results, Reviewed result. **Chenyu Zhou:** Conceptualization, Methodology, Reviewed result. **Lingchen Kong:** Model implementation, Reviewed result. **Chengqing Liu:** Analysis and interpretation of results, Reviewed result. **Qiang Yu:** Supervision, Funding acquisition, Reviewed result.

## Declaration of competing interest

The authors declare that they have no known competing financial interests or personal relationships that could have appeared to influence the work reported in this paper.

## Data availability

The authors do not have permission to share data.

## Acknowledgements

This work was supported in part by the National Natural Science Foundation of China (52172362, 52002034, 52172361), Major Science and Technology Projects of Shaanxi Province (2020ZDZX06-01-01); in part by the Fok Yingdong Young Teachers Fund Project (171103); in part by the Key Research and Development Program of Shaanxi (2020ZDLGY16-01, 2020ZDLGY16-02, 2020ZDLGY16-03, 2020ZDLGY16-04, 2021ZDLGY12-01); in part by Natural Science Basic Research Program of Shaanxi (2022JQ-543). All authors approved the final version of the manuscript.

## Appendix A. Notation

See Table A.1.

## Appendix B. Proof of the computation accuracy of the SFF algorithm

The maximum absolute error between the distances computed by the SFF exact and approximate construction algorithms in an arbitrary geometry without obstacles can be deduced. Accordingly, a theoretical proof is given to prove the computation accuracy advantage of the proposed approximate algorithm over the state-of-the-art approximate algorithms [14–17].

In such a geometry, let  $(x_L, y_L)$  denotes the coordinate of a cell, and  $(x_C, y_C)$  denotes the coordinate of the exit cell closest to it, respectively. Then, the Euclidean (exact) distance between them can be calculated by (B.1).

$$d_{SF,E} = \sqrt{(x_L - x_C)^2 + (y_L - y_C)^2} \quad (B.1)$$

(1) The error of the Neumann neighbourhood algorithm [14] is calculated by (B.2).

$$ER_N = d_{SF,N} - d_{SF,E} \quad (B.2)$$

Since  $d_{SF,N} = |x_L - x_C| + |y_L - y_C|$ , (B.2) can be rewritten as

$$ER_N = d_{SF,E} (|\cos(\varpi^i)| + |\sin(\varpi^i)| - 1) \quad (B.3)$$

Where  $\varpi^i$  is the angle between the line connecting  $(x_L, y_L)$  and  $(x_C, y_C)$  and the  $x$ -axis.

Thus,  $ER_N$  ranges in  $[0, (\sqrt{2} - 1) d_{SF,E}]$  and the maximum absolute error  $MAE_N = |(\sqrt{2} - 1) d_{SF,E}|$ .

(2) The error of the Moore neighbourhood algorithm [14] is calculated by (B.4).

$$ER_M = d_{SF,M} - d_{SF,E} \quad (B.4)$$

Since  $d_{SF,M} = \max(|x_L - x_C|, |y_L - y_C|)$ , then we have

$$ER_M = d_{SF,E} (\max(|\cos(\varpi^i)|, |\sin(\varpi^i)|) - 1) \quad (B.5)$$

Thus,  $ER_M$  ranges in  $[(\frac{\sqrt{2}}{2} - 1) d_{SF,E}, 0]$ , and the maximum absolute error  $MAE_M = |(\frac{\sqrt{2}}{2} - 1) d_{SF,E}|$ .

(3) The error of the algorithm in Huang and Guo [17] is calculated by (B.6).

$$ER_H = d_{SF,H} - d_{SF,E} \quad (B.6)$$

Since  $d_{SF,H} = \varepsilon d_{SF,N} + (1 - \varepsilon) d_{SF,M}$ , and then we have

$$ER_H = d_{SF,E} (\varepsilon (|\cos(\varpi^i)| + |\sin(\varpi^i)|) + (1 - \varepsilon) \max(|\cos(\varpi^i)|, |\sin(\varpi^i)|) - 1) \quad (B.7)$$

Introduce variable  $k_H = \frac{\min(|\cos(\varpi^i)|, |\sin(\varpi^i)|)}{\max(|\cos(\varpi^i)|, |\sin(\varpi^i)|)}$  ( $k_H \in [0, 1]$ ), (B.7) can be rewritten as

$$ER_H = d_{SF,E} \left( \frac{1}{\sqrt{1 + k_H^2}} (\varepsilon k_H + 1) - 1 \right) \quad (B.8)$$

Then, we have  $(ER_H)' = d_{SF,E} \frac{1}{(1+k_H^2)^{3/2}} (\varepsilon - k_H)$ . It means that the boundary of the error depends on the value of  $\varepsilon$  ( $\varepsilon \in [0, 1]$ ), and the error obtains the maximum only when  $\varepsilon = k_H$ . Thus its maximum ranges in  $[0, d_{SF,E} (\sqrt{2} - 1)]$ ,

and correspondingly the minimum lies between the interval  $[d_{SF,E} (\frac{\sqrt{2}}{2} - 1), 0]$ . If we set  $\varepsilon = 0.5$  as suggested in Huang and Guo [17], the error ranges in  $[0, d_{SF,E} (\frac{\sqrt{5}}{2} - 1)]$  and the maximum absolute error  $MAE_H = |d_{SF,E} (\frac{\sqrt{5}}{2} - 1)|$ .

(4) The error of the proposed algorithm can be calculated by (B.9).

$$ER_P = d_{SF,P} - d_{SF,E} \quad (B.9)$$

Recall **SFF – Construction**( $\alpha_{SF}$ ,  $C$ ,  $ST^e$ ), (B.9) can be rewritten as

$$ER_P = d_{SF,E} (\max(|\sin(\varpi^i)|, |\sin(\varpi^i)|) + \min(|\cos(\varpi^i)|, |\sin(\varpi^i)|) (1 - \exp(-(\alpha_{SF}/2) \min(|\cos(\varpi^i)|, |\sin(\varpi^i)|) / \max(|\cos(\varpi^i)|, |\sin(\varpi^i)|)))) \quad (B.10)$$

Introduce variable  $k_P$  (with the same definition as  $k_H$ ), and rewrite (B.10) as

$$ER_P = d_{SF,E} \frac{1}{\sqrt{1 + k_P^2}} (1 + k_P (1 - \exp(-(\alpha_{SF}/2) k_P))) \quad (B.11)$$

Then we obtain  $(ER_P)' = \frac{1}{(1+k_P^2)^{3/2}} (1 - k_P + \exp(-(\alpha_{SF}/2) k_P) ((\alpha_{SF}/2) (k_P + k_P^3) - 1))$ . Obviously, equation  $(ER_P)' = 0$  cannot be solved analytically [60], and the numerical solutions are  $k_P = 0.2586$  and  $0.7261$ , when  $\alpha_{SF} = 1.074$  (obtained by the GA in Section 3.1).

Thus  $ER_P$  ranges in  $[-0.0011 d_{SF,E}, 0.00061 d_{SF,E}]$ , and the maximum absolute error  $MAE_P = |-0.0011 d_{SF,E}|$ .

From the above analyses, we can conclude  $MAE_P \ll MAE_H < MAE_M < MAE_N$ , and thus the significant computation accuracy advantage of the proposed algorithm over the existing approximate algorithms in the scenarios without obstacles is theoretically proven.

**Table C.1**

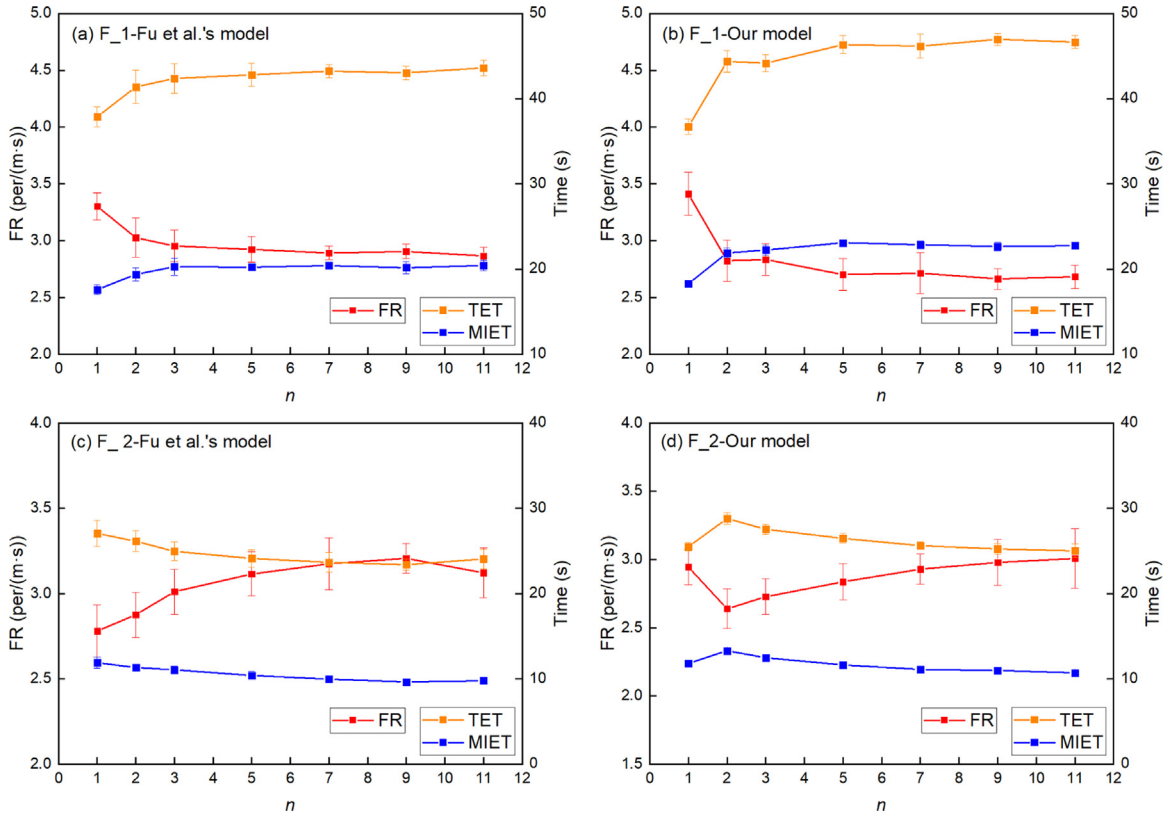
Parameter settings for the model of Kirchner and Schadschneider [14].

Parameter	Sensitivity to static field	Sensitivity to dynamic field	Friction factor	Diffusion constant of dynamic field	Decay constant of dynamic field
Symbol Value	$K_{\text{OSF}}$ 8	$K_{\text{ODF}}$ 1	$\mu_{\text{ODF}}$ 0	$\alpha_{\text{ODF}}$ 0.3	$\delta_{\text{ODF}}$ 0.3

**Table C.2**

Parameter settings in the reproduction work (Set 1) and this paper (Set 2), where the asterisk sign identifies the parameter values obtained from Fu et al. [7].

Parameter	Sensitivity to static field	Sensitivity to dynamic field	Maximum desired velocity	Steering probability	Competition relationship between pedestrians	Average competitive capacity of pedestrians
Set 1	2*	0*	5 m/s*	0.5	Inf	1
Set 2	By calibration	0*	5 m/s*	0.5	Inf	1

**Fig. D.1.** Effect of the discretization degree ( $n$ ) on the mean of individual evacuation times (MIET), the total evacuation time (TET), and the flow rate (FR) in setups F\_1 and F\_2 for our and Fu et al.'s models.

## Appendix C. Parameter settings

### C.1. The model of Kirchner and Schadschneider [14]

As suggested in [13], a high degree of sensitivity to the SFF is set to avoid the potential disturbance of the herding tendency ( $K_{\text{ODF}}$ ) and the friction effect ( $\mu_{\text{ODF}}$ ) on the results (see Table C.1). And, the discretization degree is set as 1.

### C.2. The model of Fu, et al. [7]

Through reproducing their works related to the evacuation from an empty room (one of the case studies in Fu, et al. [7]), the parameter values of Set 1 in Table C.2 are obtained (The related results are also thoroughly discussed in Appendix D). The sensitivity parameter value of the static and dynamic fields is scenario-dependent. The latter is set as 0 (the same as that in our model), and the former is determined by the calibration procedure in Section 3.2.1. The parameter values of Set 2 in Table C.2 are finally used in this paper. Prior simulations indicate the possible occurrence of jamming when Fu

et al.'s model with the chosen parameter settings is used to simulate setups M\_2 and M\_6 (bidirectional flow), and thus the (calibration and comparison) simulations related to the bidirectional flow setups are not conducted.

## Appendix D. Additional evidence on the discretization effect

There are only two differences between setups F\_1 and F\_2, i.e., the pedestrian distribution and the exit width. In setup F\_1, pedestrians are randomly distributed and the exit is 1.2 m wide, whereas pedestrians are piled up in front of the exit and the exit width is 2 m in setup F\_2.

According to Fig. D.1(a), for setup F\_1, the results of this paper accord with those of Fu, et al. [7], which justifies the used parameter settings. Qualitatively similar results are also observed in our model, shown in Fig. D.1(b). The decrease of the evacuation efficiency in Fig. D.1(a) and (b) should be ascribed to the increasing conflict number as a result of finer discretization. However, the discretization effect saturates when the discretization degree surpasses certain values. This is because orderly movement queues are formed in this situation [30].

As shown in Fig. D.1(c) and (d), for setup F\_2, a positive effect of the discretization degree on the evacuation efficiency is generally observed in both our and Fu et al.' models. Nevertheless, in our model, the evacuation efficiency first experiences a significant decrease when the discretization degree changes from  $n = 1$  to  $n = 2$  (Fig. D.1(d)), which should be attributed to the impact of conflicts among pedestrians, as indicated in Section 4.3.2.

## References

- [1] O. Hosseini, M. Maghrebi, M.F. Maghrebi, Determining optimum staged-evacuation schedule considering total evacuation time, congestion severity and fire threats, *Saf. Sci.* 139 (2021) 105211.
- [2] D. Huang, S. Lo, J. Chen, Z. Fu, Y. Zheng, L. Luo, Y. Zhuang, H. Cheng, L. Yang, Mapping fire risk of passenger-carried fire load in metro system via floor field cellular automaton, *Autom. Constr.* 100 (2019) 61–72.
- [3] M. Haghani, Optimising crowd evacuations: Mathematical, architectural and behavioural approaches, *Saf. Sci.* 128 (2020) 104745.
- [4] Y. Feng, D. Duives, W. Daamen, S. Hoogendoorn, Data collection methods for studying pedestrian behaviour: A systematic review, *Build. Environ.* 187 (2021) 107329.
- [5] D. Helbing, I. Farkas, T. Vicsek, Simulating dynamical features of escape panic, *Nature* 407 (2000) 487–490.
- [6] W.L. Wang, S.M. Lo, S.B. Liu, H. Kuang, Microscopic modeling of pedestrian movement behavior: Interacting with visual attractors in the environment, *Transp. Res. C* 44 (2014) 21–33.
- [7] Z.J. Fu, Q.H. Jia, J.M. Chen, J. Ma, K. Han, L. Luo, A fine discrete field cellular automaton for pedestrian dynamics integrating pedestrian heterogeneity, anisotropy, and time-dependent characteristics, *Transp. Res. C* 91 (2018) 37–61.
- [8] C. Burstedde, K. Klauck, A. Schadschneider, J. Zittartz, Simulation of pedestrian dynamics using a two-dimensional cellular automaton, *Physica A* 295 (2001) 507–525.
- [9] J. Zhang, W. Song, X. Xu, Experiment and multi-grid modeling of evacuation from a classroom, *Physica A* 387 (2008) 5901–5909.
- [10] S.P. Hoogendoorn, P.H.L. Bovy, Pedestrian route-choice and activity scheduling theory and models, *Transp. Res. B* 38 (2004) 169–190.
- [11] D.C. Duives, W. Daamen, S.P. Hoogendoorn, State-of-the-art crowd motion simulation models, *Transp. Res. C* 37 (2013) 193–209.
- [12] N. Pelechano, A. Malkawi, Evacuation simulation models: Challenges in modeling high rise building evacuation with cellular automata approaches, *Autom. Constr.* 17 (2008) 377–385.
- [13] K. Nishinari, A. Kirchner, A. Namazi, A. Schadschneider, Extended floor field CA model for evacuation dynamics, *IEICE Trans. Inf. Syst.* E87D (2004) 726–732.
- [14] A. Kirchner, A. Schadschneider, Simulation of evacuation processes using a bionics-inspired cellular automaton model for pedestrian dynamics, *Physica A* 312 (2002) 260–276.
- [15] B. Anvari, M.G.H. Bell, P. Angeloudis, W.Y. Ochieng, Long-range collision avoidance for shared space simulation based on social forces, *Transp. Res. Proc.* 2 (2014) 318–326.
- [16] A. Varas, M.D. Cornejo, D. Mainemer, B. Toledo, J. Rogan, V. Munoz, J.A. Valdivia, Cellular automaton model for evacuation process with obstacles, *Physica A* 382 (2007) 631–642.
- [17] H.J. Huang, R.Y. Guo, Static floor field and exit choice for pedestrian evacuation in rooms with internal obstacles and multiple exits, *Phys. Rev. E* 78 (2008) 021131.
- [18] E.W. Dijkstra, A note on two problems in connexion with graphs, *Numer. Math.* 1 (1959) 269–271.
- [19] S.P. Hoogendoorn, F.L.M. van Wageningen-Kessels, W. Daamen, D.C. Duives, Continuum modelling of pedestrian flows: From microscopic principles to self-organised macroscopic phenomena, *Physica A* 416 (2014) 684–694.
- [20] W. Song, X. Xu, B.-H. Wang, S. Ni, Simulation of evacuation processes using a multi-grid model for pedestrian dynamics, *Physica A* 363 (2006) 492–500.
- [21] U. Weidmann, Transporttechnik der Fußgänger: transporttechnische Eigenschaften des Fußgängerverkehrs, literatuauswertung, IVT Schriftenreihe 90 (1993).
- [22] A. Kirchner, H. Klüpfel, K. Nishinari, A. Schadschneider, M. Schreckenberg, Discretization effects and the influence of walking speed in cellular automata models for pedestrian dynamics, *J. Stat. Mech. Theory Exp.* 2004 (2004) P10011.
- [23] W.G. Weng, L.L. Pan, S.F. Shen, H.Y. Yuan, Small-grid analysis of discrete model for evacuation from a hall, *Physica A* 374 (2007) 821–826.
- [24] R.-Y. Guo, H.-J. Huang, A modified floor field cellular automata model for pedestrian evacuation simulation, *J. Phys. A* 41 (2008) 385104.
- [25] R.-Y. Guo, H.-J. Huang, S.C. Wong, Route choice in pedestrian evacuation under conditions of good and zero visibility: Experimental and simulation results, *Transp. Res. B* 46 (2012) 669–686.
- [26] W. Daamen, S. Hoogendoorn, Calibration of pedestrian simulation model for emergency doors by pedestrian type, *Transp. Res. Rec.* 2316 (2012) 69–75.
- [27] Y. Yuan, B. Goñi-Ros, T.P.V. Oijen, W. Daamen, S.P. Hoogendoorn, Social force model describing pedestrian and cyclist behaviour in shared spaces, in: *Traffic and Granular Flow '17*, Springer International Publishing, Cham, 2019, pp. 477–486.
- [28] G. Tang, Z. Zhao, J. Yu, Z. Sun, X. Li, Simulation-based framework for evaluating the evacuation performance of the passenger terminal building in a Ro-Pax terminal, *Autom. Constr.* 121 (2021) 103445.
- [29] X. Wang, Z. Liu, S. Loughney, Z. Yang, Y. Wang, J. Wang, Numerical analysis and staircase layout optimisation for a Ro-Ro passenger ship during emergency evacuation, *Reliab. Eng. Syst. Saf.* 217 (2022) 108056.
- [30] X. Xu, W.G. Song, H.Y. Zheng, Discretization effect in a multi-grid egress model, *Physica A* 387 (2008) 5567–5574.

- [31] R.Y. Guo, New insights into discretization effects in cellular automata models for pedestrian evacuation, *Physica A* 400 (2014) 1–11.
- [32] A. Kirchner, H. Klüpfel, K. Nishinari, A. Schadschneider, M. Schreckenberg, Simulation of competitive egress behavior: comparison with aircraft evacuation data, *Physica A* 324 (2003) 689–697.
- [33] S.P. Hoogendoorn, W. Daamen, Pedestrian behavior at bottlenecks, *Transp. Sci.* 39 (2005) 147–159.
- [34] S. Maniccam, Effects of back step and update rule on congestion of mobile objects, *Physica A* 346 (2005) 631–650.
- [35] W. Yuan, K.H. Tan, A novel algorithm of simulating multi-velocity evacuation based on cellular automata modeling and tenability condition, *Physica A* 379 (2007) 250–262.
- [36] L. Fu, W. Song, S. Lo, A fuzzy-theory-based behavioral model for studying pedestrian evacuation from a single-exit room, *Phys. Lett. A* 380 (2016) 2619–2627.
- [37] R. Huang, X. Zhao, Y. Yuan, Q. Yu, W. Daamen, Open experimental data-sets to reveal behavioural insights of high-deck coach evacuations, *Fire Technol.* (2022).
- [38] Y. Hu, J. Zhang, W. Song, N.W.F. Bode, Social groups barely change the speed-density relationship in unidirectional pedestrian flow, but affect operational behaviours, *Saf. Sci.* 139 (2021) 105259.
- [39] W. Daamen, S.P. Hoogendoorn, Free speed distributions – Based on empirical data in different traffic conditions, in: N. Waldau, P. Gattermann, H. Knoflacher, M. Schreckenberg (Eds.), in: *Pedestrian and Evacuation Dynamics 2005*, Springer Berlin Heidelberg, Berlin, Heidelberg, 2007, pp. 13–25.
- [40] S. Liu, S. Lo, J. Ma, W. Wang, An agent-based microscopic pedestrian flow simulation model for pedestrian traffic problems, *IEEE Trans. Intell. Transp. Syst.* 15 (2014) 992–1001.
- [41] R. Zhao, Y. Zhai, L. Qu, R. Wang, Y. Huang, Q. Dong, A continuous floor field cellular automata model with interaction area for crowd evacuation, *Physica A* 575 (2021).
- [42] S. Nowak, A. Schadschneider, Quantitative analysis of pedestrian counterflow in a cellular automaton model, *Phys. Rev. E* 85 (2012) 066128.
- [43] Y. Hu, X. Ren, J. Zhang, W. Song, An experimental study on the movement characteristics of a social group in unidirectional flow, *Transp. A: Transp. Sci.* (2022) 1–20.
- [44] Y. Suma, D. Yanagisawa, K. Nishinari, Anticipation effect in pedestrian dynamics: Modeling and experiments, *Physica A* 391 (2012) 248–263.
- [45] J. Zhang, W. Klingsch, A. Schadschneider, A. Seyfried, Ordering in bidirectional pedestrian flows and its influence on the fundamental diagram, *J. Stat. Mech. Theory Exp.* 2012 (2012) P02002.
- [46] E. Ronchi, P.A. Reneke, R.D. Peacock, A method for the analysis of behavioural uncertainty in evacuation modelling, *Fire Technol.* 50 (2014) 1545–1571.
- [47] M. Spaaij, D.C. Duives, V.L. Knoop, S.P. Hoogendoorn, Multiobjective calibration framework for pedestrian simulation models: A study on the effect of movement base cases, metrics, and density levels, *J. Adv. Transp.* 2019 (2019) 1–18.
- [48] W. Daamen, C. Buisson, S.P. Hoogendoorn, *Traffic Simulation and Data: Validation Methods and Applications*, CRC Press, Boca Raton, 2014.
- [49] M. Spaaij, *How to Calibrate a Pedestrian Simulation Model: An Investigation Into how the Choices of Scenarios and Metrics Influence the Calibration*, Delft University of Technology, 2017.
- [50] C. Keip, K. Ries, Dokumentation von versuchen zur personenstromdynamik, Technical Report, Project Hermes, 2009.
- [51] R. Huang, X. Zhao, Y. Yuan, Q. Yu, C. Liu, W. Daamen, Modelling pedestrian tactical and operational decisions under risk and uncertainty: A two-layer model framework, *IEEE Trans. Intell. Transp. Syst.* (2022) (under review).
- [52] Q. Xu, M. Chraibi, A. Seyfried, Anticipation in a velocity-based model for pedestrian dynamics, *Transp. Res. C* 133 (2021) 103464.
- [53] C. Dias, R. Lovreglio, Calibrating cellular automaton models for pedestrians walking through corners, *Phys. Lett. A* 382 (2018) 1255–1261.
- [54] M. Campanella, S. Hoogendoorn, W. Daamen, Improving the Nomad microscopic walker model, *IFAC Proc. Vol.* 42 (2009) 12–18.
- [55] M. Campanella, S. Hoogendoorn, W. Daamen, Quantitative and qualitative validation procedure for general use of pedestrian models, in: U. Weidmann, U. Kirsch, M. Schreckenberg (Eds.), *Pedestrian and Evacuation Dynamics 2012*, Springer International Publishing, Cham, 2014, pp. 891–905.
- [56] A. Tordeux, M. Chraibi, A. Seyfried, Collision-free speed model for pedestrian dynamics, in: V.L. Knoop, W. Daamen (Eds.), *Traffic and Granular Flow '15*, Springer International Publishing, Cham, 2016, pp. 225–232.
- [57] Q. Xu, M. Chraibi, A. Tordeux, J. Zhang, Generalized collision-free velocity model for pedestrian dynamics, *Physica A* 535 (2019) 122521.
- [58] T. Kretz, Pedestrian traffic: on the quickest path, *J. Stat. Mech. Theory Exp.* 2009 (2009) P03012.
- [59] R. Huang, X. Zhao, Y. Yuan, Q. Yu, C. Zhou, W. Daamen, Experimental study on evacuation behaviour of passengers in a high-deck coach: A Chinese case study, *Physica A* 579 (2021) 126120.
- [60] Y. Liu, Z. Fang, M.H. Cheung, W. Cai, J. Huang, An incentive mechanism for sustainable blockchain storage, *IEEE/ACM Trans. Netw.* (2022) 1–14, <http://dx.doi.org/10.1109/TNET.2022.3166459>.